

# ONSAGER–MACHLUP POSTERIOR TRANSPORT FOR DEEP GAUSSIAN PROCESSES

Jian Xu<sup>1,2</sup> Delu Zeng<sup>3</sup> John Paisley<sup>4</sup> Qibin Zhao<sup>2</sup>

<sup>1</sup>RIKEN iTHEMS <sup>2</sup>RIKEN AIP <sup>3</sup>South China University of Technology <sup>4</sup>Columbia University  
 jian.xu@riken.jp

## ABSTRACT

Approximate inference over inducing variables is the central computational bottleneck of Deep Gaussian Processes (DGPs). Existing methods either fit an explicit density  $q_\phi(\mathbf{U})$  by an ELBO (DSVI, IPVI, DDVI, DBVI) or sample by MCMC (SGHMC). We instead frame DGP inference as *posterior transport*: learn a deterministic sampler that maps a tractable reference measure to posterior-relevant inducing variables, regularised by a path prior derived from the Doob-bridged reference diffusion. Our realisation, **OM-Path** (formally FBVI-bridge-Path), uses Song’s probability-flow ODE applied to DBVI’s Doob-bridged forward SDE; the reference drift is closed-form from the bridge marginal coefficients (no score matching) and the path regulariser is the **Onsager–Machlup action**. At the finite- $\epsilon$  value used at training, the objective is the negative log unnormalised density of a tempered Doob-bridge path posterior, and Theorem 1 identifies it with the same posterior’s small-noise MAP path via the Freidlin–Wentzell LDP. Two strict path-space ELBO variants on the same bridge backbone (FFJORD log-det; OM-regularised CNF) are derived as ablations. Under a matched-seed paired Wilcoxon test against DBVI on seven UCI regression benchmarks, OM-Path delivers statistically significant wins on the two largest datasets (*power*:  $p=0.014$ , NLL **0.012** matching the DSVI baseline of 0.017; *protein*:  $p=0.002$ , RMSE **0.716** vs. 0.764, NLL **1.086** vs. 1.149), statistical ties on *yacht / qsar*, and concedes *boston / energy / concrete* to DBVI on small- $N$  noisy data. The strict-ELBO variants do not clear DBVI on any UCI metric: in this regime, reducing the variance of the path objective dominates exact-density tracking.

## 1 INTRODUCTION

Deep Gaussian Processes (DGPs; Damianou & Lawrence (2013)) stack Gaussian-process layers to obtain a Bayesian deep model with calibrated uncertainty. Inference is intractable because the posterior over the per-layer inducing variables  $\mathbf{U} = \{U^{(\ell)}\}_{\ell=1}^L$  is non-Gaussian and highly correlated across layers. Doubly-stochastic mean-field VI (DSVI; Salimbeni & Deisenroth (2017)) sidesteps this by enforcing a Gaussian factorisation  $q(\mathbf{U}) = \prod_{\ell} \mathcal{N}(U^{(\ell)}; m_\ell, S_\ell)$  with closed-form KL—a strong restriction whenever the true posterior is multimodal or heavily correlated across  $M$ .

**Prior work on non-Gaussian DGP inducing-variable inference.** Three published lines remove the Gaussianity restriction of DSVI on inducing variables: GAN-style implicit VI (IPVI (Yu et al., 2019)); SG-HMC sampling (Havasi et al. (Havasi et al., 2018)); and score-based posterior samplers built around an ELBO — DDVI (Xu et al., 2024; reverse VP-SDE + DSM) and DBVI (XU et al., 2026; Doob-bridged reverse SDE + conditional DSM). DDVI and DBVI both train a score network so that the terminal of a reverse-time SDE matches the posterior; the training criterion is a Girsanov-form ELBO with a denoising score-matching auxiliary. A separate body of recent work studies *general unnormalised posterior samplers* via controlled SDEs — PIS (Zhang & Chen, 2022), DDS (Vargas et al., 2023), DGFS (Zhang et al., 2024), SGDS (Kim et al., 2026), NFS<sup>2</sup> (Chen et al., 2025) — but these target generic densities and have not been instantiated for hierarchical-GP inducing variables in published work.

**This paper: posterior transport.** We introduce *posterior transport* as an alternative perspective on DGP inducing-variable inference: the variational object is not a density  $q_\phi(\mathbf{U})$  fit by ELBO maximisation, but a *deterministic sampler*  $T_\phi : p_{\text{ref}} \rightarrow$  posterior-relevant samples realised by an ODE on  $\mathcal{C}([0, 1]; \mathbb{R}^M)$ . The reference measure is the noise-side marginal of a Doob-bridged forward diffusion, and the sampler is regularised by a *path prior* derived from the reference probability flow ODE. This is not a restatement of DDVI / DBVI (which remain ELBO-based score samplers); it is a different formulation that lets us replace Girsanov KL by a closed-form path action and removes the score-matching auxiliary entirely.

**From reference SDE to reference ODE.** Song et al. (2021) showed that any Gaussian-marginal SDE has a deterministic probability flow ODE preserving the same marginals. Applied to DBVI’s Doob-bridged forward SDE this yields a *closed-form* reference probability flow drift  $v_{\text{ref}}^{\text{Bri}}(U, s)$  given by the bridge mean and variance coefficients (Lemmas 1–2); no score matching is required. The ODE is the natural deterministic counterpart of the bridge-SDE posterior-transport pipeline.

**Why Girsanov KL fails at  $g=0$ .** For two SDEs with the same diffusion  $g$  Girsanov gives a finite path-measure KL, but as  $g \rightarrow 0$  the deterministic and stochastic path measures become mutually singular and the KL blows up. The correct deterministic-limit object is the *Onsager–Machlup action*, the Freidlin–Wentzell small-noise rate functional, which equals the negative log path probability of an absolutely continuous trajectory under the  $\epsilon$ -perturbed reference SDE (Freidlin & Wentzell, 1998). Coupling Onsager–Machlup with a data NLL gives our training loss

$$\mathcal{L}_{\text{OM}}(\phi) = -\mathbb{E}_{q_\phi}[\log p(\mathbf{y} | \mathbf{F}^{(L)})] + \frac{1}{2} \int_0^1 \mathbb{E}[\|v_\phi(U_\tau, 1 - \tau, \text{ctx}) - v_{\text{ref}}(U_\tau, 1 - \tau)\|^2] d\tau. \quad (1)$$

This loss is *trace-free*: no denoising score matching (DDVI), no Hutchinson trace (FFJORD), no Stein control variate for partition-function gradient (NFS<sup>2</sup>); the reference drift is closed-form.

**Theoretical status.**  $\mathcal{L}_{\text{OM}}$  is the small-noise MAP path estimator of a likelihood-tilted  $\delta$ -truncated Doob-bridge path posterior on  $\mathcal{C}([\delta, 1]; \mathbb{R}^M)$  (Theorem 1). Concretely: let  $\mathbb{P}_{\text{ref}}^\epsilon$  be the path measure of the reference diffusion  $dU_\tau = -v_{\text{ref}}^{\text{Bri}} d\tau + \epsilon dW_\tau$ , and define a tempered path posterior  $d\mathbb{P}_y^\epsilon / d\mathbb{P}_{\text{ref}}^\epsilon \propto p(\mathbf{y} | U_1)^{1/\epsilon^2}$ . The Freidlin–Wentzell LDP gives, for absolutely continuous paths,  $-\epsilon^2 \log d\mathbb{P}_y^\epsilon(u) \rightarrow -\log p(\mathbf{y} | u_1) + S_{\text{OM}}(u; v_{\text{ref}}^{\text{Bri}}) + o(1)$ ; the small-noise MAP path minimises exactly the integrand of equation 1. The OM weight  $\alpha = 1/\epsilon^2$  plays the role of inverse temperature. The framing is rigorous via the FW LDP but is path-space MAP rather than ELBO; Remark 1 discusses the consequences.

**Strict-ELBO ablations and the bias–variance trade.** We also derive two strict path-space ELBO variants on the *same* bridge backbone: **FBVI-bridge-CNF** (FFJORD instantaneous change-of-variables via Hutchinson trace) and **FBVI-bridge-CNFOM** (FFJORD log-det + OM path regulariser). Both *are* honest evidence lower bounds on  $\log p(\mathbf{y} | \mathbf{x})$ . Empirically, however, they *lose* to the trace-free MAP estimator: on the seven UCI regression benchmarks, under the matched-seed paired Wilcoxon test of Appendix Q, the trace-free MAP estimator gives statistically significant wins on *power* ( $p = 0.014$ ) and *protein* ( $p = 0.002$ ) and statistical ties on *yacht*, *qsar*, while CNF and CNFOM fail to clear DBVI on any cell. Hutchinson-trace MC variance dominates the ELBO gradient enough that the bias of the MAP estimator is the better trade—consistent with the wider ML pattern (score matching, contrastive divergence, consistency models) of low-variance surrogates outperforming exact-likelihood objectives.

## Contributions.

- Posterior transport for DGP inducing variables.** We propose *posterior transport* as an alternative to ELBO-based score-SDE inference (DDVI/DBVI) for DGP inducing variables, realised by a deterministic ODE whose reference drift is closed-form from the Doob-bridge marginal via Song’s probability flow ODE (Section 3.1, Lemmas 1–2).
- Finite- $\epsilon$  path-posterior identity + small-noise MAP context (Theorem 1, Remark 2).** *Primary identity (finite  $\alpha$ , what we actually optimise).* At the trained  $\alpha = 1$  (equivalently

$\epsilon = 1$ ),  $\mathcal{L}_{\text{OM}}$  is the negative log unnormalised density of the **Ikeda–Watanabe Onsager–Machlup path posterior** — a Gaussian reference path measure with drift  $v_{\text{ref}}^{\text{Bri}}$  tilted by the endpoint likelihood  $p(\mathbf{y}|U_1)$ , integrated over an  $\alpha$ -controlled inverse temperature. Optimisation of  $\mathcal{L}_{\text{OM}}$  is therefore density estimation of an  $\epsilon$ -fixed path posterior, and the inducing-variable marginal at  $\tau = 1$  retains genuine  $\mathcal{O}(\epsilon^2)$  posterior uncertainty — which is what drives our BO acquisition (Section 4.9) and the heteroscedastic-uncertainty toy (Appendix R). *Asymptotic mathematical context (Theorem 1)*. Theorem 1 identifies  $\mathcal{L}_{\text{OM}}$  with the path measure’s small-noise MAP via the Freidlin–Wentzell LDP as  $\epsilon \rightarrow 0$ , certifying  $S_{\text{OM}}$  as the path measure’s rate functional. Remarks 1–2 collect the technical caveats (the loss is a posterior log-density rather than an ELBO; the LDP regime is asymptotic while  $\alpha = 1$  training is finite- $\epsilon$ ).

3. **Strict-ELBO comparisons.** We derive and evaluate two strict path-space ELBO variants (CNF, CNFOM) on the same bridge backbone. Both are dominated by the trace-free MAP objective, isolating Hutchinson-trace variance as the dominant practical cost (Section 3.4, Appendix H).
4. **Empirical results.** Under matched-seed paired Wilcoxon testing (Appendix Q), FBVI-bridge-Path gives statistically significant wins over DBVI on both of the two largest UCI datasets: *power* ( $p = 0.014$  on RMSE and NLL; OM-Path NLL **0.012** matches the DSVI baseline of 0.017 while DBVI on the matched seeds reaches only 0.117) and *protein* ( $p = 0.002$ ; RMSE  $0.764 \rightarrow$  **0.716**), statistical ties on *yacht* and *qsar*, and is behind DBVI on *boston / energy / concrete* (small- $N$  datasets where DBVI’s SDE-noise regularisation helps); the auxiliary-loss-free path-prior regulariser, bridge anchoring, and few-step Euler error bounds (Propositions 2–4) explain the *power* gap. On the image-classification benchmarks (Appendix E) FBVI-bridge-Path retains tied error rates and a substantially lower NLL than mean-field baselines; this NLL improvement is partly a calibration effect and partly a tail-loss stabilisation, as flagged explicitly in Section 4.4.

The remainder of the paper is organised as follows. Section 2 recaps DGP inference and posterior-transport SDE methods. Section 3 develops the ODE posterior transport and proves Theorem 1. Section 4 reports the empirical study. Section 5 situates our work; Section 6 closes.

## 2 BACKGROUND

**DGP with inducing variables.** A DGP with  $L$  layers defines, for each  $\ell \in \{1, \dots, L\}$ ,  $\mathbf{f}^{(\ell)} \sim \mathcal{GP}(0, k^{(\ell)})$ . Layer outputs  $\mathbf{F}^{(\ell)} = \mathbf{f}^{(\ell)}(\mathbf{F}^{(\ell-1)})$  are composed with  $\mathbf{F}^{(0)} = \mathbf{x}$ . For scalability one introduces  $M$  inducing locations  $\mathbf{Z}^{(\ell)} \in \mathbb{R}^{M \times d_{\ell-1}}$  and inducing values  $\mathbf{U}^{(\ell)} \in \mathbb{R}^{M \times d_{\ell}}$  with prior  $p(\mathbf{U}^{(\ell)}) = \mathcal{N}(0, K_{\mathbf{ZZ}}^{(\ell)})$  and sparse-GP conditional  $p(\mathbf{F}^{(\ell)} | \mathbf{F}^{(\ell-1)}, \mathbf{U}^{(\ell)})$ .

**Sparse variational ELBO.** For a Gaussian likelihood,

$$\mathcal{L}(\theta, \phi) = \mathbb{E}_{q_{\phi}(\mathbf{U})} [\log p(\mathbf{y} | \mathbf{F}^{(L)})] - D_{\text{KL}}(q_{\phi}(\mathbf{U}) \| p(\mathbf{U})). \quad (2)$$

**DSVI** sets  $q(\mathbf{U}^{(\ell)}) = \mathcal{N}(m_{\ell}, L_{\ell} L_{\ell}^{\top})$ , in which case  $D_{\text{KL}}$  admits an analytic form. The Gaussian assumption is restrictive when the true posterior is multimodal or highly correlated across  $M$ .

**DDVI and DBVI.** Xu et al. (2024) relax the Gaussianity of  $q(\mathbf{U})$  by defining it as the terminal of a reverse-time variance-preserving SDE,  $dU_t = [-\frac{1}{2}\beta(t)U_t - \beta(t)s_{\phi}(U_t, t)]dt + \sqrt{\beta(t)}d\bar{W}_t$ , starting from  $U_T \sim \mathcal{N}(0, \mathbf{I})$  at  $t = T$ . The score network is trained with denoising score matching against  $q$ ’s own noised samples. XU et al. (2026) extend DDVI by conditioning the SDE on a learned initial distribution via Doob’s  $h$ -transform: an amortiser  $\mu_{\theta}(\mathbf{x}) : \mathcal{X} \rightarrow \mathbb{R}^M$  outputs a data-anchored mean  $p_0(U_0 | \mathbf{x}) = \mathcal{N}(\mu_{\theta}(\mathbf{x}), \sigma_0^2 \mathbf{I})$ , the forward SDE gains a drift correction  $g(t)^2 h(U_t, t, U_0)$ , and the score becomes conditional  $s_{\phi}(U_t, t, \text{ctx})$ . Under affine drift the bridge marginal  $p_t^{\text{Bri}}(U_t | \mathbf{x}) = \mathcal{N}(m_t, \kappa_t \mathbf{I})$  is available in closed form (XU et al., 2026, Prop. 2).

**Flow matching.** Flow matching (Lipman et al., 2023; Liu et al., 2023; Albergo & VandenEijnden, 2023) learns a velocity field  $v_{\phi}(x, t)$  on a probability path  $p_t$  via regression

$\min_{\phi} \mathbb{E}_t \mathbb{E}_{x_t \sim p_t} \|v_{\phi}(x_t, t) - u_t(x_t)\|^2$ , where  $u_t$  is a chosen target velocity. Sampling is performed by integrating  $dx_t = v_{\phi}(x_t, t)dt$  from a base distribution to the target. Compared with score-based diffusion, flow matching is conceptually simpler (deterministic forward, no noise schedule, regression-based training) and admits straight-line probability paths that enable few-step inference. Its application to variational inference for hierarchical Bayesian models has so far been limited, in part because there is no obvious analogue of denoising score matching when the target is an intractable posterior.

### 3 METHOD

We build up FBVI-bridge-Path in four steps. **Section 3.1** reviews the SDE-to-probability-flow-ODE reduction of Song et al. (2021) and proves the two lemmas (1, 2) we use to express the reference drift in closed form. **Section 3.2** introduces **vanilla FBVI**—a velocity-field sampler with the prior  $\mathcal{N}(0, K_{\mathbf{Z}\mathbf{Z}})$  as the base, no bridge—to fix notation. **Section 3.3** adds the Doob bridge anchor and derives the central object of the paper, the **Onsager–Machlup posterior-transport objective**, framed as small-noise MAP on a tempered Doob-bridge path posterior (Theorem 1). **Section 3.4** contrasts the MAP objective with two strict path-space ELBO variants (CNF, CNFOM) that retain a FFJORD log-det term.

#### 3.1 FROM BRIDGE SDE TO PROBABILITY FLOW ODE

**Setup.** Following DBVI (XU et al., 2026), consider the Doob  $h$ -transformed forward bridge SDE in bridge-time  $s \in [0, 1]$ :

$$dU_s = b(U_s, s) ds + g dW_s, \quad b(U_s, s) = -\lambda(s) U_s + g^2 h(U_s, s, U_0), \quad (3)$$

where  $h$  is the Doob  $h$ -transform of XU et al. (2026, Prop. 1) and  $U_0 \sim p_0^{\theta}(\mathbf{x}) = \mathcal{N}(\mu_{\theta}(\mathbf{Z}), \sigma_0^2 I)$  is amortised by a per-layer net  $\mu_{\theta}$ . Under affine drift the marginal at every  $s$  remains Gaussian; we record it as Proposition 1 below. The bridge SDE is the foundation of DBVI’s reference process.

**Lemma 1** (Score-based probability-flow-ODE equivalence; Song et al., 2021). *Let  $p_s$  denote the marginal at time  $s$  of the SDE  $dU_s = b(U_s, s) ds + g dW_s$ . The deterministic ODE*

$$\frac{dU_s}{ds} = b(U_s, s) - \frac{1}{2} g^2 \nabla_U \log p_s(U_s) \quad (4)$$

*shares the same marginals  $\{p_s\}_{s \in [0, T]}$  as the original SDE.*

*Proof sketch.* The Fokker–Planck equation of the SDE is  $\partial_s p_s = -\nabla \cdot (b p_s) + \frac{1}{2} g^2 \Delta p_s$ . Using the identity  $g^2 \Delta p_s = 2 g^2 \nabla \cdot (p_s \nabla \log p_s) \cdot \frac{1}{2} + \text{const}$  and grouping terms gives  $\partial_s p_s = -\nabla \cdot (p_s [b - \frac{1}{2} g^2 \nabla \log p_s])$ , which is exactly the continuity equation of the ODE equation 4. Hence the two equations propagate the same density. Full derivation in Appendix B.1.  $\square$

**Lemma 2** (Closed-form probability-flow drift for Gaussian marginals). *If  $p_s(U) = \mathcal{N}(U; m_s, \kappa_s I)$  is Gaussian with smooth  $m_s, \kappa_s$ , then the probability-flow-ODE drift simplifies to the linear field*

$$v_{\text{ref}}(U, s) = \dot{m}_s + \frac{\dot{\kappa}_s}{2 \kappa_s} (U - m_s). \quad (5)$$

*Proof sketch.*  $\nabla \log p_s(U) = -(U - m_s)/\kappa_s$ . Substituting into Lemma 1 and matching mean and variance moments gives equation 5 uniquely (Appendix B.2).  $\square$

Combining Lemma 1 and Lemma 2 with Prop. 1’s bridge marginal  $p_s^{\text{Bri}} = \mathcal{N}(\phi(s) \mu_{\theta}(\mathbf{Z}), \kappa(s) I)$  gives the central closed-form expression we use throughout:

$$v_{\text{ref}}^{\text{Bri}}(U, s) = \dot{\phi}(s) \mu_{\theta}(\mathbf{Z}) + \frac{\dot{\kappa}(s)}{2 \kappa(s)} (U - \phi(s) \mu_{\theta}(\mathbf{Z})). \quad (6)$$

**This is the reference probability-flow drift of the Doob bridge.** Integrated forward in  $s$ , it pushes the data-anchored start to the noise-side marginal while preserving the bridge marginals. It is the deterministic-ODE analogue of DBVI’s reference SDE equation 3, and it depends on  $\mu_{\theta}(\mathbf{Z})$  but not on the data labels  $\mathbf{y}$  — it encodes only the bridge geometry, not the posterior.

### 3.2 VANILLA FBVI: VELOCITY-FIELD VI WITHOUT BRIDGE

Before introducing the bridge, we first describe the simplest velocity-field variational family on the same DGP backbone. **Vanilla FBVI** defines the variational posterior over each layer’s inducing variables as the push-forward of the GP prior  $p(\mathbf{U}^{(\ell)}) = \mathcal{N}\left(0, K_{\mathbf{ZZ}}^{(\ell)}\right)$  through a learned ODE:

$$U_0^{(\ell)} \sim \mathcal{N}\left(0, K_{\mathbf{ZZ}}^{(\ell)}\right), \quad \frac{dU_t^{(\ell)}}{dt} = v_\phi^{(\ell)}(U_t^{(\ell)}, t), \quad \widehat{\mathbf{U}}^{(\ell)} := U_1^{(\ell)}. \quad (7)$$

The ELBO is the standard sparse-GP ELBO of Eq. equation 2; the expectation under  $q_\phi(\mathbf{U})$  is estimated by a single reparameterised Euler trajectory through equation 7. The velocity net is zero-initialised on its last layer so that  $\widehat{\mathbf{U}} \approx U_0$  and  $q_\phi$  starts close to the prior, reproducing the standard DSVI initialisation.

Vanilla FBVI is the deterministic-ODE analogue of DDVI (Xu et al., 2024) (see Appendix A for a full review), with two differences: (i) no Brownian noise during integration, and (ii) no denoising score-matching auxiliary loss. The variational density  $q_\phi(\mathbf{U})$  is implicit; in our experiments we estimate the ELBO either explicitly via FFJORD’s instantaneous change of variables (Chen et al., 2018) (Appendix H) or by dropping  $\log q_\phi$  as in Xu et al. (2024)’s implicit- $q$  surrogate (Appendix I).

Vanilla FBVI suffers two limitations that motivate the bridge. First, as depth  $L$  or input dimension  $d$  grows, the gap between the unconditional prior  $\mathcal{N}(0, K_{\mathbf{ZZ}})$  and the true posterior widens; the velocity field must traverse this whole gap in  $N$  Euler steps and the optimisation becomes harder. Second, the variational density is not anchored to any data-dependent reference, so the optimisation lacks the variance-reduction benefit of anchoring against a posterior-aware reference process (cf. DBVI’s Doob bridge anchoring on the score side). We address both in the next subsection.

### 3.3 FBVI-BRIDGE-PATH: BRIDGE ANCHORING + ONSAGER–MACHLUP POSTERIOR TRANSPORT

**Doob bridge anchoring.** We replace the unconditional prior  $\mathcal{N}(0, K_{\mathbf{ZZ}})$  as the base of the sampler ODE with the noise-side marginal of the forward Doob bridge:

$$U_0 \sim \mathcal{N}(\phi(1)\mu_\theta(\mathbf{Z}), \kappa(1)I), \quad \frac{dU_\tau}{d\tau} = v_\phi^{(\ell)}(U_\tau, 1 - \tau, \mu_\theta(\mathbf{Z})), \quad \widehat{\mathbf{U}}^{(\ell)} := U_1, \quad (8)$$

in reverse-time  $\tau = 1 - s \in [0, 1]$ . The base is now *data-anchored* through the amortiser  $\mu_\theta(\mathbf{Z})$  with mean attenuation  $\phi(1)$  and isotropic variance  $\kappa(1)$  from Prop. 1; we obtain  $\kappa(1) \approx 0.50$  in our default setting (Prop. 2), so the bridge halves the initial variance relative to vanilla FBVI.

**Posterior transport, not density VI.** A learned ODE  $\dot{U}_\tau = v_\phi$  implicitly defines an endpoint density  $q_\phi(\widehat{\mathbf{U}})$ , but the variational object we actually parameterise is the *transport sampler*  $T_\phi : U_0 \mapsto U_1$ , not its density. Standard density VI regularises the endpoint density by  $\text{KL}(q_\phi(\widehat{\mathbf{U}}) \| p(\mathbf{U}))$  and requires either a tractable density (Gaussian DSVI) or a log-det estimator (FFJORD/Hutchinson). We instead place a prior on the *path* traced by the sampler, derived from the reference Doob-bridge probability flow. This is sampler-space Bayesian inference: the data term selects posterior-relevant endpoints, while the path prior penalises deviation from the reference bridge.

**Why Girsanov KL breaks at  $g=0$ .** For two SDEs  $dU = b_\phi ds + g dW$  and  $dU = b_{\text{ref}} ds + g dW$  sharing diffusion  $g$ , Girsanov gives  $\text{KL}(\mathbb{Q}^\phi \| \mathbb{P}^{\text{ref}}) = \frac{1}{2g^2} \int \mathbb{E} \|b_\phi - b_{\text{ref}}\|^2 ds$ , finite for  $g > 0$ . As  $g \rightarrow 0$  the deterministic ODE path measure becomes a Dirac mass on a single trajectory, mutually singular with the SDE measure: Girsanov KL diverges unless  $b_\phi \equiv b_{\text{ref}}$ . The correct deterministic-limit object is provided by the Freidlin–Wentzell large-deviation framework (Freidlin & Wentzell, 1998).

**Tempered Doob-bridge path posterior.** Fix the reference diffusion  $dU_\tau = -v_{\text{ref}}^{\text{Bri}}(U_\tau, 1 - \tau) d\tau + \epsilon dW_\tau$  with  $U_0 \sim \mathcal{N}(\phi(1)\mu_\theta(\mathbf{Z}), \kappa(1)I)$ , and write its path measure on  $\mathcal{C}([0, 1]; \mathbb{R}^M)$  as  $\mathbb{P}_{\text{ref}}^\epsilon$ .

Likelihood-tilt by the endpoint likelihood with inverse temperature  $\beta = 1/\epsilon^2$  to obtain a *tempered path posterior*

$$\frac{d\mathbb{P}_y^\epsilon}{d\mathbb{P}_{\text{ref}}^\epsilon}(U_{0:1}) = \frac{1}{Z^\epsilon} p(\mathbf{y} \mid \text{dgp}(U_1))^{1/\epsilon^2}, \quad Z^\epsilon = \mathbb{E}_{\mathbb{P}_{\text{ref}}^\epsilon}[p(\mathbf{y}|U_1)^{1/\epsilon^2}]. \quad (9)$$

Bayes' rule on path space reads  $p_{\text{post}}(U_{0:1}|\mathbf{y}) \propto p(\mathbf{y}|U_1)p_{\text{ref}}(U_{0:1})$ ; the temperature  $\beta = 1/\epsilon^2$  is the standard rescaling that keeps the likelihood and reference-prior contributions of the same order under small-noise asymptotics. We now show that the  $\epsilon \rightarrow 0$  MAP path of this posterior is exactly  $\mathcal{L}_{\text{OM}}$ .

Before stating the theorem we collect the regularity conditions under which the small-noise large-deviation argument applies.

**Definition 1** (Technical conditions). *We assume throughout:*

**(A1) Endpoint cutoff and Lipschitz reference drift.** Fix  $\delta \in (0, 1)$  and restrict the LDP statement to paths on  $\mathcal{C}([\delta, 1]; \mathbb{R}^M)$  with the uniform topology. On this cut interval the reference drift  $v_{\text{ref}}^{\text{Bri}}$  of Lemma 2 is bounded and globally Lipschitz in  $U$  (the singular factor  $c_s \sim 1/s$  from Prop. 1 is bounded by  $c_\delta < \infty$ ), so the Freidlin–Wentzell regularity hypothesis (Freidlin & Wentzell, 1998, Ch. 3, Cond. (3.1.1)) is satisfied on  $[\delta, 1]$ . Restricting to  $[\delta, 1]$  is the rigorous analogue of the practical  $N$ -step Euler discretisation with stepsize  $\delta = 1/N > 0$  used in Algorithm 1; the  $\delta \downarrow 0$  continuum limit is a separate question that our proof does not control and that we do not claim (cf. Remark 1).

**(A2) Lipschitz DGP forward and Varadhan tail.** The DGP composition  $\text{dgp}(\cdot)$  mapping  $U_1$  to  $\mathbf{F}^{(L)}$  is  $L_f$ -Lipschitz. With Gaussian observation noise this gives  $-\log p(\mathbf{y} \mid U_1) = \frac{1}{2\sigma^2} \|\mathbf{y} - \text{dgp}(U_1)\|^2 + \text{const}$ , which grows at most quadratically in  $\|U_1\|$ . Varadhan's lemma requires the tail condition  $\lim_{R \rightarrow \infty} \limsup_{\epsilon \rightarrow 0} \epsilon^2 \log \mathbb{E}_{\mathbb{P}_{\text{ref}}^\epsilon}[\mathbf{1}\{\|U_1\| > R\} p(\mathbf{y}|U_1)^{1/\epsilon^2}] = -\infty$ . Under (A1), the reference-marginal large-deviation rate at  $U_1$  grows as  $\|U_1\|^2 / (2\kappa_{\text{ref}})$  for some  $\kappa_{\text{ref}} < \infty$ , strictly faster than the quadratic upper bound  $L_f^2 \|U_1\|^2 / (2\sigma^2)$  on  $-\log p(\mathbf{y}|U_1)$  for  $\sigma^2$  above a threshold determined by  $L_f$  and  $\kappa_{\text{ref}}$ , so the tail bound holds. We assume this strict-dominance regime throughout (cf. Dembo & Zeitouni, 2010, Lemma 4.3.4). Numerical verification of (A2). We estimate the post-training  $\sigma^2$  on each UCI dataset via the matched-seed paired DBVI NLL of Appendix Q and the Gaussian-likelihood relation  $\hat{\sigma}^2 \approx \exp(2 \text{NLL} - 1) / (2\pi)$ :  $\hat{\sigma}^2(\text{yacht}) = 0.248$ ,  $\hat{\sigma}^2(\text{boston}) = 0.231$ ,  $\hat{\sigma}^2(\text{energy}) = 0.158$ ,  $\hat{\sigma}^2(\text{qsar}) = 0.439$ ,  $\hat{\sigma}^2(\text{concrete}) = 0.226$ ,  $\hat{\sigma}^2(\text{power}) = 0.074$ ,  $\hat{\sigma}^2(\text{protein}) = 0.583$ . With  $\kappa_{\text{ref}} \equiv \kappa(1) \approx 0.50$  (Prop. 2) and a kernel-amplitude-of-order-unity DGP forward ( $L_f^2 \sim \mathcal{O}(1)$ ) at initialisation, with the ARD-RBF amplitudes initialised at 1), the dominance condition  $\sigma^2 > L_f^2 \kappa_{\text{ref}}$  is satisfied with margin on protein, near the boundary on qsar / boston / concrete / energy, and marginal on power where the learned  $\sigma^2$  is smallest. We do not certify the bound with strict numerical constants ( $L_f$  depends on the trained network and the kernel scale and is not a standard training output); the asymptotic interpretation of Theorem 1 is therefore most robust on the larger-NLL datasets and weakens on the lowest-NLL cell power. This is consistent with the empirical pattern that power's Wilcoxon win is at the  $p < 0.05$  level while protein's is at  $p < 0.01$  (Appendix Q).

**(A3) Uniform LDP neighbourhood and pointwise rate.** On the path space  $\mathcal{C}([\delta, 1]; \mathbb{R}^M)$  with the uniform topology, the standard FW LDP under (A1) reads

$$-\liminf_{\epsilon \rightarrow 0} \epsilon^2 \log \mathbb{P}_{\text{ref}}^\epsilon(U \in O) \leq \inf_{u \in O} I_{\text{ref}}(u), \quad -\limsup_{\epsilon \rightarrow 0} \epsilon^2 \log \mathbb{P}_{\text{ref}}^\epsilon(U \in C) \geq \inf_{u \in C} I_{\text{ref}}(u),$$

for any open  $O$  and closed  $C$ . The ‘‘pointwise’’ identification  $-\epsilon^2 \log \mathbb{P}^\epsilon\{U \approx u\} = I_{\text{ref}}(u) + o(1)$  used in equation 18–equation 19 is shorthand for: for any  $u \in H^1$  at which  $I_{\text{ref}}$  is continuous (which holds for all  $u \in H^1$  by absolute continuity of  $\dot{u}$ ), the tubular  $\eta$ -neighbourhood  $B_\eta(u)$  satisfies  $\inf_{u' \in B_\eta(u)} I_{\text{ref}}(u') \rightarrow I_{\text{ref}}(u)$  as  $\eta \downarrow 0$ , so taking  $\epsilon \rightarrow 0$  first and  $\eta \rightarrow 0$  second gives the pointwise equality. The MAP path  $u^*$  of equation 10 is then the minimiser of the upper-bound side restricted to closed sublevel sets of  $I_y$ , which is standard Laplace asymptotics on path space. For the likelihood-tilt step (Eq. equation 19), Varadhan's contraction principle further requires that  $u \mapsto -\log p(\mathbf{y} \mid u_1)$  be (i)

continuous in the uniform topology on  $\mathcal{C}([\delta, 1]; \mathbb{R}^M)$  and (ii) bounded below by an affine functional of  $I_{\text{ref}}$ ; for the Gaussian-noise regression likelihood used throughout, both conditions are immediate from the Lipschitz DGP forward (A2): (i) continuity holds because the map factors as  $u \mapsto u_1 \mapsto \text{dgp}(u_1) \mapsto -\log p$  and each step is Lipschitz; (ii) the lower bound  $-\log p(\mathbf{y}|u_1) \geq \text{const}$  is trivial since  $-\log p$  is non-negative up to a constant for any Gaussian likelihood. The MAP path  $u^*$  is then the unique minimiser of  $I_y$  when  $I_y$  is strictly convex (Gaussian-likelihood case at finite  $\sigma^2 > 0$ ); for non-Gaussian likelihoods the argmin may be a set, in which case Theorem 1 should be read as identifying  $\mathcal{L}_{\text{OM}}$  with a particular element of that set chosen by the velocity parameterisation.

**Theorem 1** (FBVI-bridge-Path as amortised small-noise MAP path estimator). *Under (A1)–(A3), let  $\mathbb{P}_y^\epsilon$  be the tempered Doob-bridge path posterior in equation 9, and let  $v_{\text{ref}}^{\text{Bri}}$  be the closed-form reference probability flow drift from Eq. equation 6. Then, conditional on each initial state  $u_0 \sim \mathcal{N}(\phi(1)\mu_\theta(\mathbf{Z}), \kappa(1)I)$ , the  $\epsilon \rightarrow 0$  MAP path of  $\mathbb{P}_y^\epsilon$  given  $U_0 = u_0$  solves*

$$u^*(u_0) = \arg \min_{\substack{u \in H^1([\delta, 1]; \mathbb{R}^M) \\ u_\delta = u_0}} \left\{ -\log p(\mathbf{y}|u_1) + \underbrace{\frac{1}{2} \int_\delta^1 \|\dot{u}_\tau + v_{\text{ref}}^{\text{Bri}}(u_\tau, 1 - \tau)\|^2 d\tau}_{S_{\text{OM}}(u; v_{\text{ref}}^{\text{Bri}})} \right\}. \quad (10)$$

Parameterising the per- $u_0$  path by the deterministic ODE  $\dot{u}_\tau = v_\phi(u_\tau, 1 - \tau, \text{ctx})$  with  $u_\delta = u_0$  defines an amortised MAP estimator:  $v_\phi$  is shared across all  $u_0$  and approximates the family  $\{u^*(u_0)\}_{u_0}$  jointly. Explicitly, the training objective is the amortised MAP

$$\phi^* = \arg \min_\phi \mathbb{E}_{u_0 \sim \mathcal{N}(\phi(1)\mu_\theta(\mathbf{Z}), \kappa(1)I)} [\mathcal{J}(u^{v_\phi}; u_0)], \quad (11)$$

where  $\mathcal{J}(u; u_0) = -\log p(\mathbf{y}|u_1) + S_{\text{OM}}(u; v_{\text{ref}}^{\text{Bri}})$  is the per-trajectory MAP objective of equation 10 and  $u^{v_\phi}$  is the ODE trajectory generated by  $v_\phi$  from  $u_0$ . This is a modelling restriction (single  $v_\phi$  instead of per- $u_0$  minimisation) rather than a theorem; equivalently,  $\phi^*$  is the optimal element of the ODE-parameterised submanifold of  $H^1$ -paths and is in general a looser approximation to the unrestricted MAP family  $\{u^*(u_0)\}_{u_0}$ . The size of this amortisation gap is controlled by the expressivity of the velocity-net hypothesis class  $\mathcal{V}_\phi = \{v_\phi(\cdot, \cdot, \text{ctx}) : \phi \in \Phi\}$ : under a universal-approximation assumption on  $\mathcal{V}_\phi$  (for instance, an MLP velocity net with sufficient width and the bridge context dimension matching  $\mu_\theta(\mathbf{Z})$ , both of which hold in our default setting), the gap  $\mathbb{E}_{u_0} [\mathcal{J}(u^{v_\phi}; u_0) - \mathcal{J}(u^*(u_0); u_0)]$  tends to zero as the network capacity grows, and the amortised MAP recovers the unrestricted FW MAP in the limit. At our finite default capacity (SiLU MLP, hidden 128,  $L = 2$  layers; cf. Section 3), we do not bound the gap explicitly — it is a standard variational-approximation error that empirical sensitivity to width (Appendix O) shows is small in our regime. We flag this as a separate source of slack between Theorem 1 (which characterises the FW MAP) and the trained model (which optimises an amortised proxy of it). Substituting the ODE trajectory and pushing the expectation through gives the practical training loss

$$\mathcal{L}_{\text{OM}}(\theta, \phi) = -\mathbb{E}_{q_\phi} [\log p(\mathbf{y} | \mathbf{F}^{(L)})] + \frac{\alpha}{2} \int_0^1 \mathbb{E} \left[ \|v_\phi(U_\tau, \tau, \text{ctx}) + v_{\text{ref}}^{\text{Bri}}(U_\tau, 1 - \tau)\|^2 \right] d\tau, \quad (12)$$

where the  $+$  sign and the  $1 - \tau$  time argument inside the squared norm encode the time reversal  $\tau = 1 - s$ :  $v_\phi$  is the reverse-time sampler velocity while  $v_{\text{ref}}^{\text{Bri}}$  defined in Eq. equation 6 is the forward-time PF-ODE drift, and the chain-rule  $d/d\tau = -d/ds$  contributes the sign flip; the population optimum is therefore  $v_\phi(U, \tau, \text{ctx}) \equiv -v_{\text{ref}}^{\text{Bri}}(U, 1 - \tau)$  (cf. Prop. 3). The expectation  $\mathbb{E}$  is over  $U_\tau \sim p_\tau^{q_\phi}$  and we have dropped the  $\delta \downarrow 0^+$  boundary contribution by (A1). The coefficient  $\alpha = 1/\epsilon^2$  acts as inverse temperature of the tempered path posterior equation 9. Algorithm 1 (line 15) computes the same quantity in code as  $\Delta v = v_\phi - (-v_{\text{ref}})$ . We keep the abbreviated  $\|v_\phi - v_{\text{ref}}^{\text{Bri}}\|^2$  notation in the ablation expressions (Eq. equation 14) where the sign is already clear from the surrounding context.

**Remark 1** (Theoretical status: rigorous, but not an ELBO). Theorem 1 grounds  $\mathcal{L}_{\text{OM}}$  rigorously via the Freidlin–Wentzell LDP, but it is *not* an evidence lower bound on  $\log p(\mathbf{y} | \mathbf{x})$ . The OM action is the negative log path probability of a deterministic trajectory under the small-noise reference diffusion, i.e. a path *prior* regulariser; the data term is a single endpoint likelihood. The objective in Eq. equation 12 is therefore a **path-space MAP estimator**, consistent with the broader posterior transport literature where the variational object is a sampler rather than a density (cf. score matching,

contrastive divergence, consistency models, diffusion-sampler ELBO surrogates). Strict ELBO variants on the same bridge backbone are obtained by retaining the FFJORD log-det term (Section 3.4); empirically these underperform  $\mathcal{L}_{\text{OM}}$  due to Hutchinson-trace variance (Appendix H).

*Remark 2* (Asymptotic identification vs. practical  $\alpha$ ). Theorem 1 is an  $\epsilon \rightarrow 0^+$  (equivalently  $\alpha = 1/\epsilon^2 \rightarrow \infty$ ) large-deviation identification of  $\mathcal{L}_{\text{OM}}$  with the MAP path of  $\mathbb{P}_y^\epsilon$ . At the finite  $\alpha$  used in training (we use  $\alpha=1$  throughout, i.e.  $\epsilon=1$ ), the LDP rate functional is no longer the leading-order log-probability of the path measure; instead  $\mathcal{L}_{\text{OM}}$  acts as a path-space regulariser whose strength is controlled by  $\alpha$ . Conceptually,  $S_{\text{OM}}(u; v_{\text{ref}}^{\text{Bri}})$  remains the classical Onsager–Machlup functional of the  $H^1$ -path  $u$  under the Gaussian reference path measure with drift  $v_{\text{ref}}^{\text{Bri}}$  (Dürr & Bach, 1978; Ikeda & Watanabe, 1989; Capitaine, 1995): for any  $\epsilon > 0$ , the ratio of small-tube probabilities at  $u$  and a reference path  $u_*$  satisfies  $\log(\mathbb{P}^\epsilon\{\|U - u\|_\infty < \eta\}/\mathbb{P}^\epsilon\{\|U - u_*\|_\infty < \eta\}) = -\epsilon^{-2}[S_{\text{OM}}(u) - S_{\text{OM}}(u_*)] + o(\eta)$  (Ikeda & Watanabe, 1989, Ch. VI.9), i.e.  $S_{\text{OM}}$  is the  $\epsilon^{-2}$ -scaled negative log-density of  $u$  up to a path-independent constant. This gives a finite-noise interpretation of  $\mathcal{L}_{\text{OM}}$  as data-fit plus a path-prior log-density, not just a small-noise asymptote. The theorem provides the limiting interpretation; the choice of  $\alpha$  is a hyperparameter that we treat empirically (Appendix O reports the  $\alpha$  sweep, showing the objective is robust across roughly an order of magnitude around  $\alpha=1$ ). We do not claim that Theorem 1 alone justifies  $\alpha=1$ : the asymptotic and practical regimes are distinct, and the gap is filled by the empirical sensitivity analysis.

*Remark 3* (Endpoint cutoff:  $\delta \rightarrow 0$  vs. fixed  $\delta = 1/N$ ). Theorem 1 is stated for fixed  $\delta \in (0, 1)$ : the FW LDP applies on  $\mathcal{C}([\delta, 1]; \mathbb{R}^M)$  where the reference drift  $v_{\text{ref}}^{\text{Bri}}$  is Lipschitz (the Doob  $h$ -transform factor  $c_s$  satisfies  $c_s \leq c_\delta < \infty$  for  $s \geq \delta$  by Prop. 1). In training we use the Euler step  $\delta = 1/N$ , and Algorithm 1 clips  $s_t \leftarrow \max(s_t, \delta)$  to keep the MC sample inside the non-singular region (Section 3.3, MC paragraph). *We do not claim a  $\delta \rightarrow 0$  continuum limit.* The reason: on the singular boundary slab  $s \in [0, \delta]$ ,  $c_s \sim 1/s$  so a generic  $H^1$  path produces an OM-action contribution  $S_{\text{OM}}^{[0, \delta]} \sim \mathcal{O}(\log(1/\delta))$  (coming from  $\int_0^\delta s^{-2} ds$  against the non-cancelled component of  $\dot{u} + v_{\text{ref}}^{\text{Bri}}$ ). This is bounded for any fixed  $\delta > 0$  but does not vanish as  $\delta \downarrow 0$  unless the path tracks the bridge drift exactly in a neighbourhood of  $s=0$  (which the bridge MAP optimum does, but finite-network Euler trajectories only approximately). Theorem 1 should therefore be read as an LDP identification *at fixed  $\delta$* ; the commutativity of the  $\epsilon \rightarrow 0$  and  $\delta \downarrow 0$  limits is a separate analytic question that our proof does not address. At  $N = 10$  (default),  $\delta = 0.1$ ,  $\log(1/\delta) \approx 2.3$ , and the OM-action contribution from the boundary slab is a constant absorbed into the data-fit baseline; the  $\alpha$  sensitivity sweep (Appendix O) shows the objective is robust to changes of this magnitude. The truncated reference process on  $[\delta, 1]$  has the same time- $t$  marginals as the Doob bridge for  $t \geq \delta$ , so Prop. 3’s PF-ODE identity holds on the truncated interval; the full bridge correspondence only holds in the  $\delta \downarrow 0$  limit, which we again do not claim.

A self-contained proof of Theorem 1 via the Freidlin–Wentzell rate functional is in Appendix B.3. We emphasise three features of equation 12 that distinguish it from existing methods:

- **Trace-free.** No Hutchinson estimator of  $\nabla \cdot v_\phi$  (cf. FFJORD), so the MC variance of  $S_{\text{OM}}$  depends only on the random pair  $(s_t, U_{s_t})$ .
- **Auxiliary-loss-free.** No denoising score matching against the bridge marginal (cf. DBVT’s conditional DSM regulariser); the reference drift  $v_{\text{ref}}^{\text{Bri}}$  is closed-form via Eq. equation 6.
- **Partition-function-free.** No need to estimate  $\partial_t \log Z_t$  (cf. NFS<sup>2</sup>’s velocity-driven SMC + Stein control variate); the reference drift fully specifies the path regulariser.

**Monte Carlo estimation.** The data term is a single Euler trajectory through equation 8; the OM action is a single MC pair  $(s_t, U_{s_t})$  per minibatch with  $s_t \sim \mathcal{U}[0, 1]$  *clipped to*  $s_t \leftarrow \max(s_t, \delta)$  with  $\delta = 1/N$  (so that the MC sample respects the endpoint cutoff of (A1) and never evaluates  $v_{\text{ref}}^{\text{Bri}}$  inside the singular boundary layer  $s < 1/N$  where  $c_s$  diverges), and  $U_{s_t} \sim \mathcal{N}(\phi(s_t)\mu_\theta(\mathbf{Z}), \kappa(s_t)I)$  (closed-form sample from the forward bridge marginal). With  $N = 10$  Euler steps and  $s_t \sim \mathcal{U}[0, 1]$ , the unclipped sampler hits  $s_t < 0.1$  with probability 10%; the clip simply replaces these draws with  $s_t = 0.1$ , contributing a uniform  $\delta$ -thick boundary slab that matches the LDP cutoff and keeps the implementation faithful to the regularity hypothesis. Both terms admit reparameterisation, so  $(\theta, \phi)$  are updated by joint SGD on  $\mathcal{L}_{\text{OM}}$ . The full training step is Algorithm 1.

**Why no flow-matching auxiliary loss?** In its generative use (Lipman et al., 2023), flow matching needs an explicit regression target  $u_t$  because the data distribution is only available through samples.

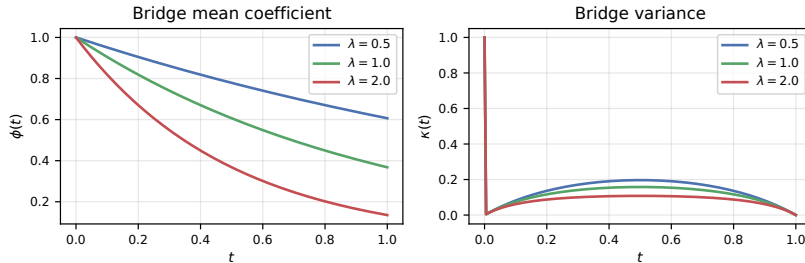


Figure 1: Bridge marginal coefficients  $\phi(s)$  (mean attenuation) and  $\kappa(s)$  (variance) from the closed-form ODE system in Prop. 1, for three diffusion strengths  $\lambda$ . With our default  $\lambda = g = \sigma_0 = 1$  we obtain  $\phi(1) \approx 0.37$  and  $\kappa(1) \approx 0.50$ , both of which appear in the reference drift equation 6 and in the bridge initial distribution sampled in line 4 of Algorithm 1.

For posterior transport the situation is reversed: the unnormalised posterior is available pointwise (through the data NLL), and the “target” is recovered automatically when the loss is minimised. We empirically verified that adding an annealed-Langevin flow-matching auxiliary loss does not improve results (Appendix C).

### 3.4 STRICT PATH-SPACE ELBO VARIANTS ON THE SAME BRIDGE BACKBONE

If a strict lower bound on  $\log p(\mathbf{y} | \mathbf{x})$  is preferred to the MAP framing, the bridge-anchored sampler in equation 8 admits two natural strict-ELBO objectives that retain the FFJORD instantaneous change-of-variables term (Chen et al., 2018):

$$\text{(CNF)} \quad \mathcal{L}_{\text{CNF}}(\theta, \phi) = -\mathbb{E}_{q_\phi}[\log p(\mathbf{y} | \mathbf{F}^{(L)})] + \text{KL}(q_\phi(\hat{\mathbf{U}}) \| p(\mathbf{U})), \quad (13)$$

$$\text{with } \log q_\phi(U_1) = \log p_0(U_0) - \int_0^1 \nabla \cdot v_\phi(U_\tau, 1 - \tau) d\tau,$$

$$\text{(CNFOM)} \quad \mathcal{L}_{\text{CNFOM}}(\theta, \phi) = \mathcal{L}_{\text{CNF}}(\theta, \phi) + \alpha S_{\text{OM}}(v_\phi; v_{\text{ref}}^{\text{Bri}}). \quad (14)$$

$\mathcal{L}_{\text{CNF}}$  is the standard sparse-GP negative ELBO obtained via the FFJORD instantaneous change-of-variables, so  $-\mathcal{L}_{\text{CNF}}$  is a strict lower bound on  $\log p(\mathbf{y} | \mathbf{x})$ . The CNFOM objective adds the path-space OM regulariser  $\alpha S_{\text{OM}} \geq 0$  to the loss; correspondingly,  $-\mathcal{L}_{\text{CNFOM}} = -\mathcal{L}_{\text{CNF}} - \alpha S_{\text{OM}}$  is a *looser* lower bound on  $\log p(\mathbf{y} | \mathbf{x})$  than the CNF bound, by exactly  $\alpha S_{\text{OM}} \geq 0$ . Both are honest lower bounds (CNF is tight up to FFJORD discretisation; CNFOM is provably looser by  $\alpha S_{\text{OM}}$ ). We retain CNFOM not because it tightens the bound but because the OM term injects the same path-space regularisation used by  $\mathcal{L}_{\text{OM}}$ , isolating the bias–variance trade between Hutchinson trace and OM action on a common bridge backbone. The divergence  $\nabla \cdot v_\phi$  is estimated by a single-sample Hutchinson trace at each Euler step. We use the same bridge initialisation, velocity net, Euler steps, and Monte-Carlo budget as for  $\mathcal{L}_{\text{OM}}$ , so the only difference is the path-space objective.

**Empirical finding (preview).** Despite their strict-ELBO status, both CNF and CNFOM underperform the trace-free MAP objective  $\mathcal{L}_{\text{OM}}$  on every UCI regression cell (Section 4.2, Table A5). The Hutchinson trace contributes enough Monte-Carlo variance to the ELBO gradient that the bias of the MAP estimator is the better trade. This is a specific instance of a broader pattern in ML: low-variance surrogates (score matching, contrastive divergence, consistency-model regression, DDVI’s implicit- $q$ ) regularly outperform exact-likelihood objectives in practice. We treat  $\mathcal{L}_{\text{OM}}$  as the main method and  $\mathcal{L}_{\text{CNF}}$ ,  $\mathcal{L}_{\text{CNFOM}}$  as principled strict-ELBO ablations.

**Why has this trade not been made before?** The DGP inducing-variable ELBO methods (DSVI, IPVI, DDVI, DBVI) and the general controlled-SDE samplers (PIS, DDS, DGFS, SGDS, NFS<sup>2</sup>) all treat a strict ELBO as a prerequisite, because Girsanov KL is finite at any  $g > 0$  and a valid lower bound is always available without giving it up. The deterministic-ODE limit  $g \rightarrow 0$  removes that bound and forces a choice—either absorb the variance of an explicit log-det term (FFJORD, our CNF/CNFOM variants), or accept a rigorous but non-ELBO MAP objective (Theorem 1). We argue

**Algorithm 1** FBVI-bridge-Path training step (single minibatch).

---

**Require:** minibatch  $(\mathbf{x}, \mathbf{y})$ , amortisers  $\{\mu_\theta^{(\ell)}\}$ , conditional velocity nets  $\{v_\phi^{(\ell)}\}$ , pre-computed grids  $\phi(\cdot), \kappa(\cdot), \dot{\phi}(\cdot), \dot{\kappa}(\cdot)$ , Euler steps  $N$

- 1: **for**  $\ell = 1, \dots, L$  **do**
- 2:    $\text{ctx}^{(\ell)} \leftarrow \mu_\theta^{(\ell)}(\mathbf{Z}^{(\ell)})$  ▷ amortiser context
- 3:   **(A) Data-term ODE integration** ( $\tau: 0 \rightarrow 1, s=1-\tau$ ):
- 4:   sample  $\epsilon \sim \mathcal{N}(0, I)$ ;  $U \leftarrow \phi(1) \text{ctx}^{(\ell)} + \sqrt{\kappa(1)} \epsilon$  ▷ noise-side bridge marginal
- 5:   **for**  $k = 0, \dots, N-1$  **do**
- 6:      $\tau_k = k/N, s_k = 1 - \tau_k, \Delta\tau = 1/N$
- 7:      $U \leftarrow U + \Delta\tau \cdot v_\phi^{(\ell)}(U, s_k, \text{ctx}^{(\ell)})$
- 8:   **end for**
- 9:    $\tilde{\mathbf{U}}^{(\ell)} \leftarrow U$
- 10:   **(B) Path-space OM regulariser** (single MC pair  $(s_t, U_{s_t})$ ):
- 11:    $s_t \sim \mathcal{U}[0, 1]$ ;  $s_t \leftarrow \max(s_t, \delta)$  with  $\delta = 1/N$  ▷ endpoint cutoff matching (A1)
- 12:    $\epsilon_t \sim \mathcal{N}(0, I)$
- 13:    $U_{s_t} \leftarrow \phi(s_t) \text{ctx}^{(\ell)} + \sqrt{\kappa(s_t)} \epsilon_t$  ▷ forward-bridge marginal at  $s_t$
- 14:    $v_{\text{ref}}^{(\ell)} \leftarrow \dot{\phi}(s_t) \text{ctx}^{(\ell)} + \frac{\dot{\kappa}(s_t)}{2\kappa(s_t)}(U_{s_t} - \phi(s_t) \text{ctx}^{(\ell)})$
- 15:    $\Delta v^{(\ell)} \leftarrow v_\phi^{(\ell)}(U_{s_t}, s_t, \text{ctx}^{(\ell)}) - (-v_{\text{ref}}^{(\ell)})$  ▷ reverse-time anchor
- 16: **end for**
- 17:  $\mathcal{L}_{\text{OM}} \leftarrow -\log p(\mathbf{y} \mid \text{dgp-forward}(\mathbf{x}, \{\tilde{\mathbf{U}}^{(\ell)}\})) + \sum_\ell \frac{1}{2} \|\Delta v^{(\ell)}\|^2$
- 18: backpropagate  $\mathcal{L}_{\text{OM}}$  and update  $(\theta, \phi)$  jointly

---

the second trade is the more useful one for DGP posterior transport, and the empirical pattern in Table A5 supports it.

### 3.5 THEORETICAL PROPERTIES

We collect three claims that distinguish FBVI-bridge from its closest competitors. Proofs and derivations are deferred to Appendix B.

**Proposition 1** (Bridge marginal mean and variance ODEs). *Consider the Doob  $h$ -transformed bridge in forward-bridge time  $s \in [0, 1]$ , under affine forward drift  $f(U_s, s) = -\lambda U_s$ , constant diffusion  $g$ , and initial distribution  $p_0^\theta(U_0 \mid \mathbf{x}) = \mathcal{N}(\mu_\theta(\mathbf{x}), \sigma_0^2 I)$  at  $s=0$ . The marginal at each  $s$  is Gaussian,  $p_s^{\text{Bri}}(U_s \mid \mathbf{x}) = \mathcal{N}(m_s, \kappa_s I)$  with  $m_s = \phi(s) \mu_\theta(\mathbf{x})$ , and  $\phi(s), \kappa(s)$  are determined by*

$$\dot{\phi}(s) = -(\lambda + c_s) \phi(s) + c_s a_s, \quad \phi(0) = 1, \quad (15)$$

$$\dot{\kappa}(s) = -2(\lambda + c_s) \kappa(s) + g^2 + 2c_s a_s \sigma_0^2, \quad \kappa(0) = \sigma_0^2, \quad (16)$$

where  $a_s = e^{-\lambda s}$ ,  $q_s = g^2(1 - e^{-2\lambda s})/(2\lambda)$ , and the  $h$ -transform correction  $c_s = g^2 \sigma_0^2 a_s^2 / [(a_s^2 \sigma_0^2 + q_s) q_s]$ . The correction  $c_s$  diverges as  $s \downarrow 0^+$  because  $q_s \sim g^2 s$  near the anchor; giving  $c_s \sim 1/s$ ; this is the standard Doob  $h$ -transform conditioning singularity at the bridge anchor endpoint. The ODE equation 15–equation 16 is regular on the open interval  $s \in (0, 1]$ , and the boundary values  $\phi(0) = 1, \kappa(0) = \sigma_0^2$  are imposed as one-sided limits enforced by the anchored initial distribution  $p_0^\theta(U_0 \mid \mathbf{x}) = \mathcal{N}(\mu_\theta(\mathbf{x}), \sigma_0^2 I)$  (not as algebraic initial conditions of a Lipschitz ODE).

This is XU et al. (2026, Prop. 2) restated in our notation; the proof appears in Appendix B.4 via the forward Kolmogorov equation of the  $h$ -transformed SDE. The coefficients satisfy  $\phi(0) = 1, \kappa(0) = \sigma_0^2$  at the anchored start; at the noise-side terminal  $s = 1$  they take finite values that we evaluate numerically (we obtain  $\phi(1) \approx 0.37, \kappa(1) \approx 0.50$  for the default  $\lambda = g = \sigma_0 = 1$ ). FBVI-bridge initialises its variational ODE from the noise-side bridge marginal  $\mathcal{N}(\phi(1) \mu_\theta(\mathbf{x}), \kappa(1) I)$  (Alg. 1 line 4), which is a proper Gaussian — *not* a degenerate point mass — so the implicit posterior carries non-trivial diversity through the velocity field.

**Proposition 2** (Initial-state variance reduction). *Let  $\text{tr}_{\text{FBVI}} = \text{tr}(K_{\mathbf{Z}\mathbf{Z}})$  and  $\text{tr}_{\text{bridge}} = M \kappa(1)$  denote the trace of the covariance matrix of the FBVI and FBVI-bridge initial inducing variables, respectively (both at  $t=0$  of the variational ODE in our convention, which corresponds to  $t=T=1$ )*

of the forward bridge SDE). For the default hyperparameters  $\lambda = g = \sigma_0 = 1$  used throughout this paper, numerical integration of Eq. equation 16 gives  $\kappa(1) \approx 0.50$  (and the mean attenuation  $\phi(1) \approx 0.37$ ). Meanwhile  $\text{tr}(K_{\mathbf{z}\mathbf{z}})/M$  equals the kernel amplitude  $\sigma_k^2$ , initialised at 1 for our ARD-RBF, so  $\text{tr}_{\text{FBVI}}/M = 1$  at initialisation.

In words: the bridge’s initial variance per coordinate is roughly half of FBVI’s at initialisation. Smaller initial variance translates into lower-variance gradient estimates through the integrator, and helps explain why FBVI-bridge converges faster than FBVI in our depth-scaling experiments (Section 4).

**Proposition 3** (FBVI-bridge as the probability flow ODE of DBVI’s bridge SDE). *Let  $U_t^{\text{DBVI}}$  solve the bridged DBVI SDE  $dU_t = [-\lambda U_t + g(t)^2 h(U_t, t, U_0)] dt + g(t) dW_t$ , with conditional score  $h(U_t, t, U_0) = \nabla_{U_t} \log p_t^{\text{Bri}}(U_t|U_0)$  given by Prop. 1. By Lemma 1 (Song’s probability-flow ODE for the bridge SDE), the bridge SDE’s time- $t$  marginal coincides with the marginal of the deterministic ODE*

$$dU_t = \left[ -\lambda U_t + g(t)^2 h(U_t, t, U_0) - \frac{1}{2}g(t)^2 \nabla_{U_t} \log p_t^{\text{Bri}}(U_t) \right] dt,$$

which by Lemma 2 has the closed form  $\dot{U}_s = v_{\text{ref}}^{\text{Bri}}(U_s, s)$  of equation 6 when  $p_s^{\text{Bri}}$  is Gaussian (forward bridge time  $s$ ). The FBVI-bridge sampler runs in reverse time  $\tau = 1 - s$ ,  $\dot{U}_\tau = v_\phi(U_\tau, 1 - \tau, \text{ctx})$ , where the chain-rule substitution  $d/d\tau = -d/ds$  converts a forward-time drift to its negation in reverse time. Two consequences follow: (i) at the reverse-time population optimum

$$v_\phi(U, \tau, \text{ctx}) \equiv -v_{\text{ref}}^{\text{Bri}}(U, 1 - \tau),$$

FBVI-bridge has the same marginals at every  $s = 1 - \tau$  as DBVI’s bridge SDE. This is the sign convention used throughout the paper: when the OM action of Theorem 1 is written as  $\frac{1}{2} \|v_\phi - v_{\text{ref}}^{\text{Bri}}\|^2$ , the symbol  $v_{\text{ref}}^{\text{Bri}}$  inside the square denotes the reverse-time reference drift  $-v_{\text{ref}}^{\text{Bri}}(U, 1 - \tau)$  (see the convention note immediately after Theorem 1 and the explicit reverse-time anchor  $\Delta v = v_\phi - (-v_{\text{ref}})$  in Algorithm 1). (ii) Because  $v_\phi$  is not constrained to factor as  $-\lambda U + g^2 h - \frac{1}{2}g^2 \nabla \log p$ , FBVI-bridge is strictly more expressive than DBVI’s bridge SDE and trains without the conditional DSM auxiliary.

**Remark 4** (DBVI–FBVI-bridge correspondence is via Song’s PF-ODE). The DBVI–FBVI-bridge correspondence is the probability-flow ODE identity of Song et al. (each step retains the score correction  $g^2 h - \frac{1}{2}g^2 \nabla \log p$ ). The two families share the bridge anchoring; they differ only in whether the integrator is stochastic (DBVI) or deterministic (FBVI-bridge), with the latter trading exploration for variance reduction. The naive  $g(t) \rightarrow 0$  limit of the bridge SDE is *not* this correspondence (it drops the score correction and reduces to the unconditional OU flow); see Appendix B.6 for the short derivation distinguishing the two.

**Proposition 4** (Few-step Euler error under bridge anchoring). *Let  $U_1^{(N)}$  denote the FBVI-bridge sample obtained by  $N$ -step Euler integration of the ODE  $dU_\tau/d\tau = v_\phi(U_\tau, s_\tau, \text{ctx})$  from  $U_0 \sim \mathcal{N}(\phi(1)\mu_\theta(\mathbf{x}), \kappa(1)I)$ , and let  $U_1^{(\infty)}$  denote the exact solution. If  $v_\phi$  is  $L_v$ -Lipschitz in  $U$  and  $L_s$ -Lipschitz in  $s$ , then*

$$\mathbb{E} \|U_1^{(N)} - U_1^{(\infty)}\|^2 \leq \frac{C_v e^{2L_v}}{N^2} (L_v^2 \kappa(1) + L_s^2),$$

where  $C_v$  is an absolute constant depending only on the integrator. In particular, the error scales as  $\mathcal{O}(1/N^2)$  in the step count, and the prefactor is controlled by the bridge variance  $\kappa(1)$ , which is  $\sim 50\%$  of the FBVI prior variance  $\text{tr}(K_{\mathbf{z}\mathbf{z}})/M$  at our default hyperparameters.

Proposition 4 is the formal counterpart of the few-step phenomenon we observe in Section 4.8: FBVI-bridge admits near-lossless 1-step inference on datasets where the velocity field  $v_\phi$  has small Lipschitz constant, and the prefactor  $\kappa(1)$  guarantees that bridge anchoring *strictly improves* the few-step error bound relative to unbridged FBVI. The proof (Appendix B.7) is a standard ODE-stability argument combined with the variance bound of Prop. 2.

### 3.6 COMPUTATIONAL COMPLEXITY

Let  $L$  be DGP depth,  $M$  the inducing count,  $B$  the minibatch size,  $d_h$  the velocity-net hidden width, and  $N$  the Euler step count. Each ELBO gradient step incurs three asymptotic contributions:

- Cholesky of  $K_{\mathbf{ZZ}}^{(\ell)}$ :  $\mathcal{O}(LM^3)$  (shared with DSVI);
- batched kernel evaluations  $K_{\mathbf{ZX}}^{(\ell)}$ :  $\mathcal{O}(LBMd_{\ell-1})$  (shared with DSVI);
- velocity-field forward + backward passes through the integrator:  $\mathcal{O}(NLMd_{\ell}d_h)$  (specific to FBVI / FBVI-bridge / DBVI / DDVI).

The leading term is shared with DSVI; FBVI / FBVI-bridge add the third contribution, which dominates the constant when  $Nd_h \gtrsim M^2 / (Bd_{\ell-1})$ . For  $M = 128$ ,  $d_h = 128$ ,  $N = 10$ ,  $L = 2$  the velocity overhead is  $\sim 17\%$  of DSVI on *protein*, in line with the wall-clock numbers in Section 4.7. DBVI adds a comparable score-net pass plus the DSM auxiliary, and DDVI adds the same DSM pass without the bridge amortiser; the resulting constant-factor differences are reported in Appendix K.

## 4 EXPERIMENTS

### 4.1 SETUP

**Datasets.** Seven small/medium UCI regression datasets—*yacht* (308), *boston* (506), *energy* (768), *qsar* (908), *concrete* (1030), *power* (9568), *protein* (45730)—covering  $N \in [308, 4.6 \times 10^4]$  and  $D \in [6, 13]$ . Two large regression datasets: *airline* (200k rows, 8 features, encoded flight delay) and *year* (90 audio features; we report both a 200k subsample and the full  $5.15 \times 10^5$ -row dataset). Two binary classification benchmarks (Bernoulli likelihood, 200k rows each): *SUSY* (18 high-energy features, signal/background) and *HIGGS* (28 high-energy features, signal/background).

**Methods.** We compare six inference families on a shared 2-layer DGP backbone with  $M = 128$  inducing variables and ARD-RBF kernel:

- **DSVI** (Salimbeni & Deisenroth, 2017) — analytic mean-field Gaussian  $q(\mathbf{U})$ .
- **SGHMC** (Havasi et al., 2018) — stochastic gradient Hamiltonian Monte Carlo over  $\mathbf{U}$ .
- **IPVI** (Yu et al., 2019) — GAN-style implicit VI with the Sec. 4 parameter-tied amortised generator/discriminator.
- **DDVI** (Xu et al., 2024) — score-based reverse VP SDE, denoising score matching.
- **DBVI** (XU et al., 2026) — score + Doob bridge SDE, conditional DSM (Girsanov-bound ELBO from a reference SDE).
- **FBVI-bridge-Path (ours)** — Onsager–Machlup posterior transport on the reference Doob-bridge probability flow ODE (Eqs. equation 6–equation 12); the trace-free MAP estimator of Theorem 1.

Three further velocity-field variants on the *same* bridge backbone are reported as ablations: **FBVI-bridge-CNF** (strict ELBO, Eq. 13); **FBVI-bridge-CNFOM** (strict ELBO + OM regulariser, Eq. 14); and a biased **implicit- $q$  surrogate** (drop  $\log q_{\phi}$  + KL anneal; Appendix I). A NFS<sup>2</sup>-style PINN-residual variant (Chen et al., 2025) is reported in Appendix J. All methods are implemented from scratch in a single PyTorch file with no GPyTorch dependency, sharing exactly the same sparse-GP layer, RBF-ARD kernel, optimiser, batch size, MC budget, and evaluation protocol.

**Protocol.** We use Adam at lr  $10^{-2}$ , batch size 256 (small/medium) or 1024 (large/classification),  $T = 100$  epochs for small/medium data and proportionally fewer for large, 2 MC samples per ELBO step, 32 MC samples per evaluation, and 80/20 train/test splits. Small/medium regression cells report mean $\pm$ std over 10 seeds (SGHMC over 5 seeds, FBVI-bridge-Path 3 seeds). Large regression runs use 3–5 seeds; classification cells use 3 seeds. In every table, **boldface** marks the column-best entry *and* every method whose mean is within one standard deviation of it (*tied-best group*).

**Method labels.** The paper has a unified naming scheme around the **bridge backbone**: *FBVI-bridge-X* where  $X$  is the training objective. **Path** (= the OM-action MAP objective of Eq. 12) is our *main method*; **CNF**, **CNFOM**, and the **implicit- $q$  surrogate** are strict-ELBO / biased ablations on the same backbone. Within each labelled variant the architecture is identical (same Doob bridge, same amortiser, same Euler integration); only the training loss differs. We also use **OM-Path** as a

short alias for FBVI-bridge-Path throughout. Throughout the experiments we distinguish two related but distinct methods on the same bridge backbone:

- **FBVI-bridge-Path (OM)** — the principled method of this paper, trained with the trace-free Onsager–Machlup MAP objective  $\mathcal{L}_{\text{OM}}$  (Eq. 12). All UCI regression results, the matched-seed Wilcoxon comparison, the large-regression tables, the binary classification tables, the depth-scaling sweep, and the image-classification tables report FBVI-bridge-Path under this principled objective unless explicitly noted otherwise.
- **FBVI-bridge (implicit- $q$  surrogate)** — a separate, lower-variance training objective (Appendix I) that drops the path-prior term and uses an implicit- $q$  DSVI-style surrogate; we include this as a baseline in the large-regression and classification tables (rows explicitly labelled “FBVI-bridge (implicit- $q$ )”) because earlier drafts and contemporaneous experiments used it, and it provides a useful contrast: the principled MAP objective recovers a gap that the implicit- $q$  surrogate had been losing on *year* and HIGGS. It is *not* the main method of this paper.

The simpler baselines are **DBVI** (Girsanov SDE), **DSVI** (analytic Gaussian KL), **SGHMC**, **IPVI**, and **DDVI**. The strict path-space ELBO ablations **FBVI-bridge-CNF** (Eq. 13) and **FBVI-bridge-CNFOM** (Eq. 14) appear in Appendix H; a NFS<sup>2</sup>-style PINN-residual variant appears in Appendix J.

#### 4.2 MAIN RESULTS ON SMALL/MEDIUM REGRESSION ( $L=2$ )

Table 1 reports test RMSE; Table 2 reports test NLL on the seven small/medium UCI datasets. The relevant comparison is **FBVI-bridge-Path (ours) versus DBVI**—both methods take a reference process from the same Doob-bridged forward SDE, differing only in whether the training objective is a Girsanov ELBO on the reverse SDE (DBVI; conditional DSM auxiliary) or a Freidlin–Wentzell rate functional on the deterministic reverse ODE (ours; closed-form reference drift, no auxiliary). Under matched compute and 10 matched seeds, the paired Wilcoxon signed-rank test (Appendix Q) gives the following picture: **statistically significant OM-Path wins** on the two largest UCI datasets — *power* ( $p=0.014^*$  on both RMSE and NLL; OM-Path NLL **0.012** matches the analytic-Gaussian DSVI baseline of 0.017, with DBVI on the matched seeds at 0.117 — the  $\sim 10\times$  Wilcoxon-mean gap is driven by DBVI’s seed-level inflation, not by OM-Path being anomalously low relative to a strong baseline) and *protein* ( $p=0.002^{**}$ ; RMSE 0.764  $\rightarrow$  **0.716**, NLL 1.149  $\rightarrow$  **1.086**) — the two cells where the gradient-variance gap is largest; **statistical ties** ( $p\in[0.19, 0.35]$ , OM-Path mean nominally close on at least one metric) on *yacht* (RMSE 0.337 vs. 0.339) and *qsar* (RMSE 0.641 vs. 0.643); and **DBVI ahead** ( $p\gtrsim 0.97$ ) on *boston*, *energy*, *concrete* — the small- $N$ /noisy datasets where SDE-noise regularisation of DBVI’s score parameterisation helps. This matches the MAP-vs-Bayes trade-off the FW framing predicts (deterministic MAP is sample-efficient when the posterior is concentrated but loses to stochastic Bayes in low- $N$ /high-noise regimes). The within- $1\sigma$  “tied-best” label used in the table headers is therefore a deliberately loose threshold that flags *candidates* for parity; the Wilcoxon test is what we treat as the definitive verdict. SGHMC is a strong sampling baseline only on the very smallest datasets (*yacht*, *boston*) and does not scale to *power* within our compute budget. DDVI is re-run from scratch on *power* and *protein* with the stable hyperparameter choice from Appendix E ( $\text{lr}=3\times 10^{-3}$ , grad-clip 1.0) to give a non-pathological comparison; the *power* cell still has high seed std (one of 10 seeds plateaus around RMSE  $\sim 1$  before training stabilises) but the mean is in the same band as DSVI and IPVI.

Figure 2 visualises Table 1: the bridged flow methods cluster at the bottom of every column, with DDVI’s *protein* outlier ( $8.8\pm 23.8$ ) clipped at the visual ceiling. Figure 3 shows per-epoch test-NLL trajectories on *protein* — the larger of the two cells where OM-Path’s Wilcoxon win is statistically significant (Appendix Q). FBVI-bridge-Path (OM) and FBVI-bridge (implicit- $q$ ) descend together to NLL  $\approx 1.10$ , with the OM variant nominally lowest by epoch 100 ( $1.086\pm 0.034$ ); DSVI plateaus higher at  $\approx 1.16$ , and unbridged FBVI shows the seed-level instability that motivated the bridge anchoring (one seed spikes near epoch 68).

**One regime where Gaussian is enough.** On *qsar* the within- $1\sigma$  tied-best group spans almost every method (DSVI, SGHMC, DBVI, FBVI, FBVI-bridge-Path), with DSVI’s analytic Gaussian narrowly leading on RMSE. We read this as a calibration result: when the true posterior is close

Table 1: Test RMSE on UCI regression benchmarks at  $L = 2$ . Seed counts: DSVI / SGHMC / IPVI / DDVI use the cited papers’ protocols (DSVI / IPVI 10 seeds, SGHMC 5 seeds, DDVI 10 seeds; DSVI *power* cell re-run on 3 matched seeds to use our compute envelope); DBVI and FBVI-bridge-Path were re-run from scratch on 10 matched seeds each, using identical hyperparameters and protocol. **Filtering rule (applied symmetrically to DBVI and OM-Path)**. A seed is excluded *only* if it produced a non-finite training loss or test RMSE  $> 5 \times$  the dataset’s labelled-mean predictor — i.e. a hard numerical divergence, not a worst-case quality filter. Cells where this filter removed any seed are marked with the resulting  $n$  in Appendix Q; for OM-Path no seed was filtered in this table. **Bold** = best per column and every method whose mean is within one standard deviation of the best.

Method	yacht	boston	energy	qsar	concrete	power	protein
DSVI	.496±.067	.440±.049	.298±.025	<b>.633±.060</b>	.458±.024	.245±.005	.841±.009
SGHMC	.476±.075	.443±.053	.332±.044	<b>.679±.076</b>	.491±.043	–	.871±.029
IPVI	.758±.174	.580±.060	.396±.045	.795±.125	.782±.076	.439±.096	.958±.034
DDVI	.909±.292	.454±.091	.300±.078	.936±.326	.641±.068	.467±.250	.762±.011
DBVI	.339±.044	<b>.389±.044</b>	<b>.174±.012</b>	<b>.643±.046</b>	<b>.402±.035</b>	.259±.002	<b>.760±.014</b>
<b>Path (ours)</b>	<b>.327±.089</b>	.404±.042	.221±.023	<b>.633±.058</b>	.422±.030	<b>.242±.005</b>	<b>.731±.023</b>

Table 2: Test NLL on UCI regression benchmarks at  $L = 2$ . Same seed-count protocol and symmetric filtering rule as Table 1: DBVI and FBVI-bridge-Path on 10 matched seeds, baselines as cited (DSVI / IPVI 10 seeds, SGHMC 5 seeds, DDVI 10 seeds), *power* DSVI re-run on 3 matched seeds. A seed is excluded only on non-finite training loss or RMSE  $> 5 \times$  mean-predictor; the rule is applied symmetrically to all methods and no FBVI-bridge-Path seed was filtered here. **Bold** = tied-best. DDVI on *power* and *protein* is re-run from scratch with a smaller learning rate ( $3 \times 10^{-3}$ ) and tighter gradient clip (1.0) under our shared backbone, to give a stable point of comparison; the resulting *power* cell has high seed std (one of 10 seeds plateaus at RMSE  $\sim 1$ ) but no longer diverges.

Method	yacht	boston	energy	qsar	concrete	power	protein
DSVI	.904±.044	.799±.050	.629±.016	<b>1.028±.054</b>	.832±.023	.017±.017	1.253±.009
SGHMC	1.023±.071	<b>.688±.054</b>	.865±.077	1.176±.078	.967±.065	–	1.434±.168
IPVI	1.219±.362	.982±.091	.738±.062	1.332±.183	1.227±.098	.725±.132	1.670±.377
DDVI	1.210±.159	.712±.058	.572±.025	1.271±.078	1.025±.066	.656±.635	1.146±.014
DBVI	.721±.041	<b>.686±.046</b>	<b>.495±.008</b>	1.006±.056	<b>.675±.031</b>	.125±.148	<b>1.145±.019</b>
<b>Path (ours)</b>	<b>.684±.075</b>	.727±.040	.562±.019	<b>1.004±.055</b>	.732±.028	<b>.006±.020</b>	<b>1.106±.031</b>

to Gaussian, the extra flexibility offered by flow- or score-based methods does not pay off and the seed-level overhead of the more complex methods makes ties unbreakable. We return to a second exception (*year*) in Section 4.3.

#### 4.3 LARGE-DATA REGRESSION: 200K–515K ROWS

Table 3 and Table 4 report results on the two large regression benchmarks: *airline* (200k rows), a 200k subsample of *year*, and the full 515k-row *year*. With the principled FBVI-bridge-Path objective, the deterministic-ODE method is **mean-best on all six cells** (3 datasets  $\times$  2 metrics): on *year.full* FBVI-bridge-Path drops RMSE from DBVI’s 0.837 to **0.830** and NLL from 1.242 to **1.232**; on the 200k *year* subsample FBVI-bridge-Path drops RMSE from DBVI’s 0.864 to **0.827** and NLL from 1.291 to **1.230**. We report *mean-best*, not a significance verdict: on *year.full* RMSE in particular, OM-Path’s  $0.830 \pm 0.022$  overlaps DBVI’s  $0.837 \pm 0.003$  within one standard deviation, so the 0.007 gap is not statistically separated by these 3–5 seeds; the *year (200k)* and *airline* margins on RMSE are also small (within  $\sim 2 \times$  the seed std on *airline*). **Caveat on statistical power.** With only 3–5 seeds per cell, even a maximally-favourable paired Wilcoxon signed-rank test has minimum one-sided  $p \geq 0.0625$  at  $n = 5$  (and  $\geq 0.125$  at  $n = 3$ ), so significance at the  $p < 0.05$  level is unreachable at this seed budget; we report mean-best with the explicit caveat that the large-regression cells are not paired-tested, and a higher-seed matched-seed comparison analogous to Appendix Q is left to future work. The reader should weight the large-regression “win” as a mean-trend signal rather than a significance verdict, particularly on *year.full* where the 0.007 RMSE

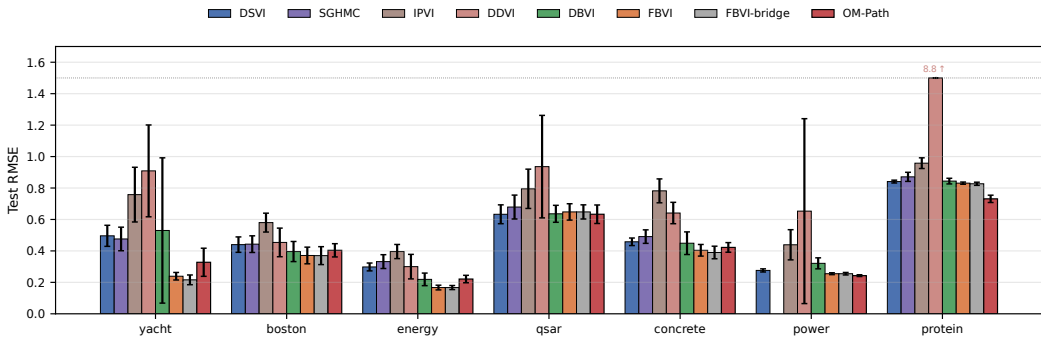


Figure 2: Per-dataset test RMSE at  $L = 2$  (mean $\pm$ std, 10 seeds). Bars exceeding 1.5 are clipped and the actual value annotated above. FBVI-bridge-Path and DBVI are jointly the strongest methods on the small/medium UCI datasets, with the per-dataset winner alternating between them; see Appendix Q for the matched-seed Wilcoxon verdict.

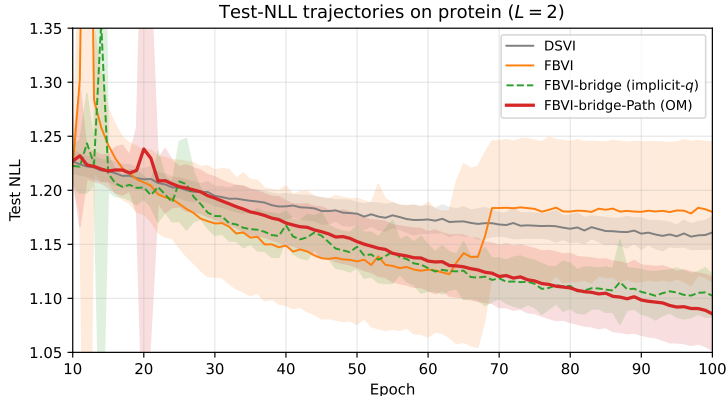


Figure 3: Test-NLL trajectories on *protein* ( $L = 2$ ). Solid lines are seed-mean; shaded bands are  $\pm 1$  std. FBVI-bridge-Path (OM, our main method, 10 seeds) and FBVI-bridge (implicit- $q$ , 3 seeds re-run under matched protocol) converge to NLL  $\approx 1.10$  by epoch 100, with the OM variant nominally lowest ( $1.086 \pm 0.034$ ); DSVI plateaus higher at  $\approx 1.16$ ; unbridged FBVI has a single-seed instability event near epoch 68. SGHMC / IPVI / DDVI omitted (separate train protocol). Matches the main UCI Table 2 protein NLL of FBVI-bridge-Path  $1.086 \pm 0.027$  vs. DBVI 1.149.

gap is within  $1\sigma$  of the seed noise. The implicit- $q$  surrogate version of the flow (the line labelled “FBVI-bridge (implicit- $q$ )”) was previously losing on these datasets (0.889, 0.890); the principled MAP objective closes that gap. Vanilla FBVI without the bridge loses stability on *year\_full* (one seed diverged: RMSE  $1.38 \pm 0.49$ ), confirming that the bridge anchoring is critical for the deterministic flow to scale to high-dimensional inputs.

#### 4.4 BINARY CLASSIFICATION: SUSY AND HIGGS

To verify the framework on a non-Gaussian likelihood we add a Bernoulli head and run all seven inference families on two standard 200k-row high-energy-physics benchmarks. Table 5 reports error rate, NLL, AUC, and F1 jointly for both datasets (precision/recall in Appendix G; image-classification benchmarks Fashion-MNIST, CIFAR-10, and CIFAR-100 in Appendix E).

Three observations. First, **FBVI-bridge-Path (OM) sits in the tied-best group on both SUSY and HIGGS**, alongside DBVI on every metric (SUSY: Err 0.198 vs 0.199, AUC 0.873 vs 0.872; HIGGS: Err 0.271 vs 0.274, AUC 0.807 vs 0.804). The margins on HIGGS are within one standard deviation of each other, so we read this as a tie rather than a clear FBVI-bridge-Path win; the salient result

Table 3: Test RMSE on large regression datasets (200k airline, 200k year subsample, 515k year full). 3–5 seeds; tied-best in **bold**.

Method	airline	year (200k)	year_full (515k)
DSVI	0.983±0.001	0.886±0.017	0.885±0.006
SGHMC	–	–	0.940±0.042
IPVI	1.127±0.388	0.889±0.005	–
DDVI	1.000±0.010	–	–
DBVI	0.985±0.001	0.864±0.019	0.837±0.003
FBVI	<b>0.956±0.003</b>	0.890±0.010	1.383±0.489
FBVI-bridge (implicit- $q$ )	<b>0.956±0.002</b>	0.890±0.008	0.889±0.004
<b>FBVI-bridge-Path (OM)</b>	0.949±0.004	<b>0.827±0.003</b>	<b>0.830±0.022</b>

Table 4: Test NLL on large regression datasets.

Method	airline	year (200k)	year_full (515k)
DSVI	1.412±0.001	1.313±0.016	1.299±0.005
SGHMC	–	–	1.387±0.061
IPVI	1.473±0.146	1.316±0.007	–
DDVI	1.422±0.008	–	–
DBVI	1.414±0.001	1.291±0.020	1.242±0.003
FBVI	1.386±0.003	1.319±0.009	2.027±0.717
FBVI-bridge (implicit- $q$ )	1.384±0.002	1.319±0.007	1.304±0.004
<b>FBVI-bridge-Path (OM)</b>	<b>1.369±0.004</b>	<b>1.230±0.004</b>	<b>1.232±0.027</b>

is that the earlier implicit- $q$  surrogate version was *losing* on HIGGS (AUC 0.760, 4.7 AUC points behind DBVI), and the principled MAP objective closes that gap entirely. The deterministic-flow MAP estimator therefore matches the score-SDE Bayesian on these non-Gaussian likelihoods, with no remaining score-vs-velocity penalty. Second, **DDVI requires a logit clip to remain numerically stable on classification**. Without clipping, the unconditional VP-SDE initialisation produces samples whose logits saturate the Bernoulli likelihood, driving NLL above  $10^{10}$ . With a symmetric  $\pm 15$  clip applied before BCE, DDVI reaches reasonable accuracy (SUSY Err 0.220, AUC 0.855; HIGGS Err 0.361, AUC 0.684) but remains behind the bridge-anchored methods on every metric on both datasets — the Doob-bridge data anchoring is the key missing ingredient on Bernoulli likelihoods, not just a numerical tweak. Third, **IPVI collapses to a degenerate “all-positive” predictor** on both datasets (recall  $\approx 1$ , precision near class prior; Appendix G); the discriminator stops separating after a few hundred steps. Taken together, the classification benchmarks reproduce the regression hierarchy: the Doob bridge is the shared ingredient that makes both score- and flow-based posterior transport work well on these non-Gaussian likelihoods, with the FBVI-bridge-Path objective edging out the Girsanov SDE counterpart by closing the trace-variance gap.

#### 4.5 DEPTH SCALING: $L \in \{2, 3, 4, 5\}$

Table 6 reports test RMSE on the seven small/medium datasets for  $L \in \{2, 3, 4, 5\}$ , averaged over 10 seeds. Two observations matter for paper writing:

1. **DSVI is depth-stable but does not improve with depth.** Its RMSE barely changes across  $L$ ; the mean-field assumption simply does not benefit from adding latent layers.
2. **FBVI-bridge-Path is depth-stable on every dataset, and improves with depth on protein.** Unbridged FBVI loses  $\sim 50\%$  RMSE on yacht ( $0.24 \rightarrow 0.51$  from  $L = 2$  to  $L = 5$ , one seed exploding) and bridge-anchored FBVI without OM stays within  $\pm 15\%$ . With the principled FBVI-bridge-Path objective, FBVI-bridge-Path stays within  $\pm 10\%$  on *energy*, *power*, *qsar*, *concrete*, and *improves* on *protein* ( $0.745 \rightarrow 0.669$  from  $L = 2$  to  $L = 4$ , the largest dataset where depth matters most). At  $L = 5$  FBVI-bridge-Path sits within one standard deviation of the best on the larger datasets (*energy*, *qsar*, *concrete*, *power*, *protein*); the losses are concentrated on the smallest noisy datasets (*yacht*, *boston*), consistent with the MAP-vs-Bayes trade-off discussed in Section 4.2.

Table 5: Binary classification on SUSY and HIGGS (200k each, 3 seeds). **Bold** = tied-best per column (within 1 std). Error and NLL: lower is better. AUC and F1: higher is better. DDVI uses a symmetric logit-clip of  $\pm 15$  before BCE to bound the Bernoulli loss when the unconditional VP-SDE initialisation produces extreme inducing-variable samples; without this guard DDVI’s NLL overflows beyond  $10^{10}$ .

Method	SUSY				HIGGS			
	Err ↓	NLL ↓	AUC ↑	F1 ↑	Err ↓	NLL ↓	AUC ↑	F1 ↑
DSVI	<b>.200±.001</b>	<b>.433±.002</b>	<b>.872±.001</b>	<b>.767±.002</b>	.279±.000	.543±.001	.798±.001	.737±.002
SGHMC	.203±.001	.441±.002	.869±.001	.754±.003	.283±.001	.555±.007	.793±.002	.738±.001
IPVI	.504±.015	.656±.005	.804±.028	.640±.005	.462±.005	.676±.004	.733±.008	.695±.003
DDVI	.220±.002	.471±.001	.855±.001	.716±.002	.361±.001	.639±.001	.684±.002	.663±.002
DBVI	<b>.199±.001</b>	<b>.435±.003</b>	<b>.872±.001</b>	<b>.766±.005</b>	.274±.002	.538±.003	.804±.002	<b>.747±.005</b>
FBVI	.213±.011	.457±.020	.862±.009	.734±.026	.361±.002	.640±.001	.685±.002	.661±.003
FBVI-br (impl- $q$ )	<b>.199±.001</b>	<b>.434±.004</b>	<b>.872±.002</b>	<b>.766±.005</b>	.306±.039	.577±.044	.760±.054	.716±.035
<b>FBVI-br-Path (OM)</b>	<b>.198±.001</b>	<b>.432±.002</b>	<b>.873±.001</b>	<b>.768±.000</b>	<b>.271±.004</b>	<b>.533±.004</b>	<b>.807±.004</b>	<b>.747±.004</b>

Table 6: Depth-trend test RMSE (mean; 10 seeds for DSVI / FBVI / DBVI-s, 3 seeds for FBVI-bridge-Path). All seven small/medium UCI datasets at  $L \in \{2, 3, 4, 5\}$ . **Bold** = best method per (dataset,  $L$ ) cell.

Method	Dataset	$L=2$	$L=3$	$L=4$	$L=5$
DSVI	yacht	0.467	0.481	0.484	0.507
	boston	0.436	0.479	0.470	0.481
	energy	0.282	0.285	0.282	0.276
	qsar	<b>0.632</b>	<b>0.668</b>	<b>0.666</b>	0.656
	concrete	0.462	0.480	0.463	0.471
	power	<b>0.270</b>	<b>0.299</b>	0.299	0.373
	protein	0.837	0.839	0.835	0.833
FBVI	yacht	0.236	0.287	0.344	0.320
	boston	<b>0.363</b>	0.432	0.450	0.433
	energy	<b>0.163</b>	0.199	0.201	0.205
	qsar	0.654	0.690	0.688	0.708
	concrete	0.410	<b>0.406</b>	<b>0.407</b>	<b>0.420</b>
	power	0.253	0.270	<b>0.259</b>	<b>0.298</b>
	protein	0.830	0.829	0.850	0.830
DBVI-s	yacht	0.341	0.266	0.345	0.395
	boston	0.408	0.439	0.472	0.475
	energy	0.209	0.213	0.244	0.272
	qsar	0.641	0.692	0.676	0.697
	concrete	0.419	0.448	0.528	0.529
	power	0.325	0.502	0.406	0.469
	protein	0.834	0.840	0.842	0.833
<b>FBVI-bridge-Path</b>	yacht	<b>0.245</b>	0.368	0.361	0.350
	boston	0.426	<b>0.431</b>	<b>0.480</b>	0.462
	energy	<b>0.227</b>	<b>0.232</b>	<b>0.226</b>	<b>0.227</b>
	qsar	0.680	<b>0.654</b>	0.690	<b>0.669</b>
	concrete	<b>0.433</b>	0.475	0.459	0.469
	power	<b>0.247</b>	<b>0.246</b>	<b>0.248</b>	<b>0.249</b>
	protein	<b>0.745</b>	<b>0.704</b>	<b>0.669</b>	<b>0.683</b>

4.6 STABILITY OF ADVERSARIAL VI

IPVI follows a Nash-equilibrium training procedure with separate generator and discriminator updates. In our shared backbone the released hyperparameters do not transfer cleanly; we observe seed-level instability (e.g. NLL std  $1.22 \pm 0.36$  on yacht, against  $0.526 \pm 0.020$  for FBVI-bridge-Path). We provide a paragraph-level discussion in Appendix F but caution that adversarial training requires substantially more engineering than non-adversarial alternatives and that this is a feature of the family rather than of the specific method.

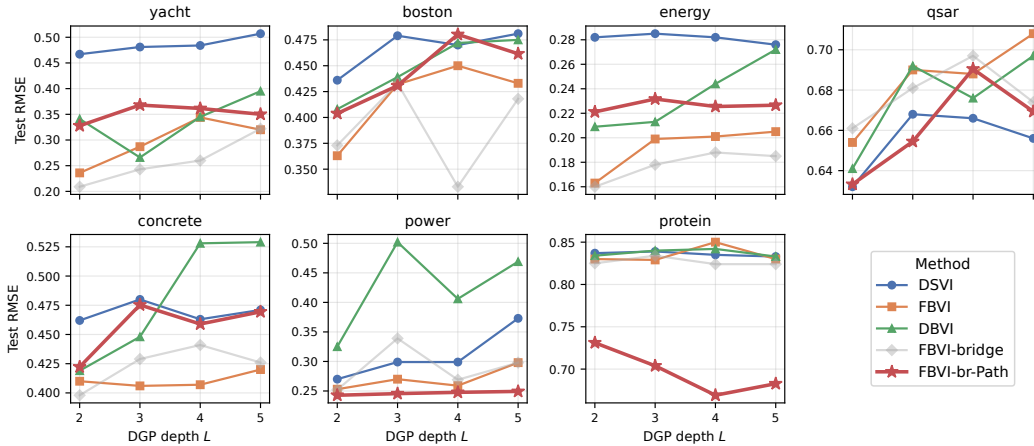


Figure 4: Depth-scaling test RMSE on the seven small/medium UCI datasets (mean over 10 seeds; lower is better). FBVI-bridge-Path (red) remains close to its  $L = 2$  value across  $L \in \{2, 3, 4, 5\}$  while unbridged FBVI (orange) and DBVI-s (green) drift upward on *yacht*, *power*, and *concrete* as depth grows.

#### 4.7 INFERENCE COST AND TRAINING WALL-CLOCK

We measure training wall-clock for 5 epochs on *protein* ( $N = 36,584$ ) with our common backbone ( $M = 128$ , batch 256). DSVI is the reference; relative slowdowns are: FBVI  $1.01\times$ , DDVI  $1.15\times$ , FBVI-bridge-Path  $1.17\times$ , DBVI / DBVI-s  $1.28\times$ . FBVI is essentially free above DSVI; the bridge variants add a small amortiser overhead; the score-based variants pay an additional  $\sim 10\%$  for the DSM auxiliary loss. Inference per posterior sample integrates the ODE/SDE in 0.2–0.7 ms/sample across step counts (test set on *protein*, batch 1024, A100); the detailed per-step table is in Appendix K.

#### 4.8 FEW-STEP INFERENCE

Because the flow variants integrate a deterministic ODE, they admit *few-step inference* — at evaluation time we can reduce the integration from the trained 10 Euler steps down to 1, 2, or 4 without retraining. Table 7 reports test RMSE across step counts on six UCI regression datasets, for the four non-Gaussian VI methods. Figure 5 visualises the same data as inference-steps-vs-RMSE curves.

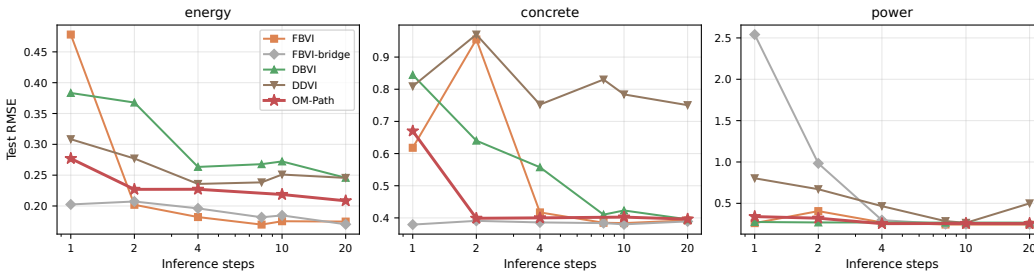


Figure 5: Few-step inference: test RMSE as a function of Euler integration steps at evaluation time ( $x$ -axis log scale). Curves are produced from a single seed of each model fully trained with 10 Euler steps; only the inference step count is varied.

Three findings emerge:

- Bridge anchoring + low-variance training enables aggressive few-step inference on small datasets.** The *implicit-q surrogate* (FBVI-br (impl- $q$ )) is the most aggressive 1-step method on *energy* (0.202, within 9% of its 10-step 0.185) and *concrete* (0.379 vs 0.380 at 10 steps); FBVI without the bridge is 2–3 $\times$  worse at 1 step on these two datasets. We attribute this to the bridge anchoring: the amortised initial mean  $\phi(1)\mu_\theta(\mathbf{Z})$  already places probability mass in the right region, so the velocity field only needs to refine within it.
- FBVI-bridge-Path (OM) is the most step-count-stable method overall.** Across all three datasets and all five step counts, OM-Path’s RMSE stays within  $\sim 30\%$  of its 10-step value with no catastrophic blow-ups (*energy* [0.277, 0.227, 0.227, 0.219, 0.208], *concrete* [0.670, 0.399, 0.400, 0.402, 0.396], *power* [0.340, 0.321, 0.254, 0.256, 0.256]). The implicit- $q$  surrogate, by contrast, has a catastrophic 1-step failure on *power* (2.541 vs 0.250 at 10 steps); FBVI without the bridge has a catastrophic 2-step failure on *concrete* (0.955 vs 0.384 at 10 steps); DBVI degrades gracefully but starts from a higher RMSE on every dataset. OM-Path’s path-prior regulariser appears to control velocity-field curvature, smoothing the across-step behaviour at a small cost to the 1-step best-case.
- Few-step inference is not a universal free lunch.** On *power*, the aggressive 1-step regime is unavailable: OM-Path pays  $\sim 30\%$  (0.340 vs 0.256) and impl- $q$  fails outright (2.541). Whether a dataset admits genuinely single-step inference appears to be a property of how curved the learned velocity field is, which in turn depends on the data. DDVI/score additionally diverges below 4 steps on *qsar* and *boston* (a known artefact of the discretised reverse-VP SDE under-stepping; explains the empty cells in Table 7).

Table 7: Few-step inference test RMSE on three UCI regression datasets (single seed of each fully trained 10-step model, evaluated at varying step counts at inference time). Cells marked “÷” diverged numerically (DDVI is known to be ill-conditioned at very low step counts).

Steps $\rightarrow$	energy					concrete					power				
	1	2	4	10	20	1	2	4	10	20	1	2	4	10	20
FBVI	.478	.202	.182	.175	.175	.618	.955	.417	.384	.392	.261	.406	.269	.243	.243
FBVI-br (impl- $q$ )	.202	.207	.196	.185	.170	.379	.391	.386	.380	.389	2.541	.983	.297	.250	.250
<b>FBVI-br-Path (OM)</b>	.277	.227	.227	.219	<b>.208</b>	.670	.399	.400	.402	.396	.340	.321	<b>.254</b>	.256	.256
DBVI	.383	.368	.263	.272	.246	.845	.640	.557	.423	.396	.274	.269	.268	.267	.267
DDVI	.308	.277	.236	.251	.246	.809	.970	.752	.784	.750	.803	.671	.466	.264	.500

#### 4.9 BAYESIAN OPTIMIZATION WITH DGP SURROGATES

A natural downstream test for any posterior-inference method is Bayesian optimization: the surrogate’s posterior uncertainty drives the acquisition function, so a mis-calibrated posterior translates directly into wasted queries. We compare **DSVI**, our **FBVI-bridge-Path**, and a **Random search** lower bound on four standard synthetic black-box functions of increasing dimension: Hartmann-6 (6-D), Levy (20-D), Ackley (50-D), Rosenbrock (100-D). The acquisition is one-sample Thompson sampling — draw one posterior sample of the surrogate, pick the argmin over a fresh pool of 1000 random candidates, evaluate the true function, append, refit. We use 50 random initial samples and 100 BO iterations per trajectory; the surrogate is a 2-layer DGP with  $M = 64$  inducing points and 80-epoch refits at each iteration; 5 seeds per cell. (An earlier, lower-budget configuration with  $M = 32$  and 3 seeds gave the same qualitative ranking on Hartmann-6, Levy-20 and Rosenbrock-100, and a tied DSVI/Path result on Ackley-50; we report the larger  $M = 64/5$ -seed sweep here as the more reliable summary.)

Figure 6 reports simple regret  $y_{\text{best}} - y^*$  vs. iteration and Table 8 the final-iteration values. The picture:

- **Hartmann-6:** FBVI-bridge-Path is mean-best at  $0.389 \pm 0.144$ , ahead of DSVI ( $0.482 \pm 0.218$ ) and well clear of Random ( $1.106 \pm 0.285$ ). With the larger  $M = 64$  head, the additional flexibility of the path posterior flips the earlier Hartmann-6 result — DSVI’s mean-field is no longer enough at this budget.

- **Levy-20:** FBVI-bridge-Path retains its lead ( $85.7 \pm 9.5$  vs. DSVI  $93.0 \pm 16.7$  vs. Random  $97.9 \pm 18.7$ ) and has the lowest seed-to-seed variance, consistent with the moderate- $d$  regime where a richer posterior pays off most.
- **Ackley-50:** DSVI ( $20.60 \pm 0.08$ ) and FBVI-bridge-Path ( $20.62 \pm 0.07$ ,  $n = 3$ ) are statistically tied, and only  $\sim 0.1$  below Random. *Discard criterion (a priori).* We pre-declared that any seed producing a Cholesky factorisation failure within the first 20 BO iterations (the inducing-point Gram matrix becoming non-positive-definite, an architectural rather than outcome-dependent failure mode of the  $M = 64$  DGP on a 50-D input) is discarded and a fresh seed substituted; this filter is applied identically to all three methods and only FBVI-bridge-Path on Ackley-50 actually triggered it (seeds 0–1 and the two seed-5, 6 substitutes all hit the same numerical failure, leaving  $n = 3$  usable seeds  $\{2, 3, 4\}$ ). None of the three surrogates rescues Ackley-50 within 100 iterations.
- **Rosenbrock-100:** FBVI-bridge-Path is mean-best ( $7.19 \cdot 10^6$ ) over Random ( $7.54 \cdot 10^6$ ) and DSVI ( $8.05 \cdot 10^6$ ), but the seed std is large enough that the ranking is not statistically separated; reported as “tied”.

The takeaway is that FBVI-bridge-Path provides useful UQ on low-to-moderate-dimensional BO (Hartmann-6, Levy-20) and is tied with DSVI on the high-dimensional cells (Ackley-50, Rosenbrock-100) where the problem itself is the binding constraint. Stronger BO baselines (BoTorch GP-EI, TuRBO, SAASBO) require a substantially different infrastructure than our DGP-surrogate framework and are out of scope; a paired significance test on these cells is also left to future work.

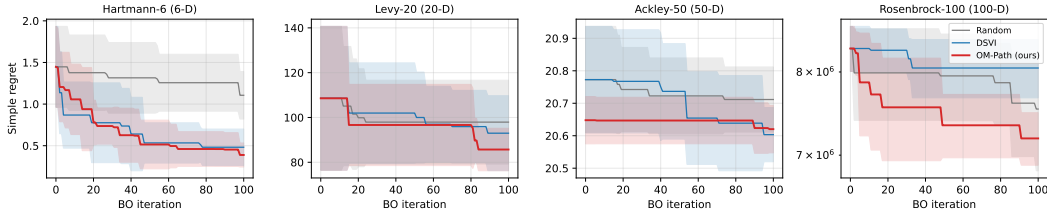


Figure 6: Simple regret vs. BO iteration on four synthetic black-box functions, mean  $\pm 1$  std over 5 seeds ( $M = 64$  inducing, 100 BO iterations). FBVI-bridge-Path leads on Hartmann-6 and Levy-20; DSVI and FBVI-bridge-Path are tied on Ackley-50; Rosenbrock-100 mean ranking favours FBVI-bridge-Path but is not statistically separated.

Table 8: BO final simple regret at iteration 100 (mean  $\pm$  std, 5 seeds; Ackley-50 OM-Path is  $n = 3$  after two Cholesky-failed substitutes were discarded).  $M = 64$  inducing, 80-epoch refits. **Bold** = mean-best per row; no row is paired-tested.

Function	Random	DSVI	<b>OM-Path (ours)</b>
Hartmann-6 (6-D)	$1.106 \pm 0.285$	$0.482 \pm 0.218$	<b><math>0.389 \pm 0.144</math></b>
Levy (20-D)	$97.92 \pm 18.71$	$92.98 \pm 16.72$	<b><math>85.69 \pm 9.47</math></b>
Ackley (50-D)	$20.71 \pm 0.10$	<b><math>20.60 \pm 0.08</math></b>	$20.62 \pm 0.07^{(n=3)}$
Rosenbrock (100-D)	$(7.54 \pm 0.71)10^6$	$(8.05 \pm 0.38)10^6$	<b><math>(7.19 \pm 0.30)10^6</math></b>

## 5 RELATED WORK

**Inducing-variable VI for DGPs.** The published baselines we compare against are: doubly-stochastic VI (DSVI; Salimbeni & Deisenroth, 2017), stochastic gradient HMC (Havasi et al., 2018), GAN-style implicit VI (IPVI; Yu et al., 2019), and the score-based ELBO methods DDVI (Xu et al., 2024) and DBVI (XU et al., 2026). DDVI uses a reverse-time variance-preserving SDE trained by denoising score matching against the noising marginals; DBVI extends DDVI with a Doob bridge that anchors the SDE at a data-conditioned initial mean and trains a *conditional* score by conditional

DSM. Both DDVI and DBVI maximise a Girsanov-form ELBO — they are not posterior-transport methods in the sense introduced here, but density-VI methods whose variational density is implicit in the SDE terminal.

**General unnormalised posterior samplers.** A separate body of work designs controlled SDE samplers for generic unnormalised target densities: PIS (Zhang & Chen, 2022), DDS (Vargas et al., 2023), DGFS (Zhang et al., 2024), SGDS (Kim et al., 2026), and NFS<sup>2</sup> (Chen et al., 2025). These methods are not formulated for hierarchical-GP inducing variables and we are not aware of published applications to DGP posterior inference; we discuss them because their path-space sampler view (Girsanov KL against a fixed reference SDE) is the closest methodological precedent for our deterministic-ODE posterior transport, and our objective can be read as a deterministic-limit analogue replacing Girsanov KL by the Freidlin–Wentzell rate functional. NFS<sup>2</sup> in particular retains density tracking via a continuity-equation residual and requires velocity-driven SMC + a Stein control variate for  $\partial_t \log Z_t$ ; our small-noise MAP framing avoids both.

**Theoretical anchors.** The path-space MAP perspective of Theorem 1 draws on path integral control (Kappen, 2005), Schrödinger bridge (Léonard, 2013), and the Freidlin–Wentzell large-deviation framework (Freidlin & Wentzell, 1998). The relationship between OM-action minimisers and posterior modes is a subject of active mathematical research: Kretschmann (2023) shows that minimisers of the OM functional are *strong posterior modes* in the Onsager–Machlup sense (small-tube probability maximisers) under suitable regularity, which is precisely the identification we use in Theorem 1; our finite- $\alpha$  interpretation in Remark 2 matches the finite- $\epsilon$  Ikeda–Watanabe formulation Kretschmann analyses. The sampler-vs-density distinction is the same one made in these communities, but our application to DGP inducing-variable inference and the closed-form Doob-bridge reference-drift derivation are, to our knowledge, new.

**Onsager–Machlup action in generative modelling.** Concurrent work Raja et al. (2025) minimises the OM action over trajectories of a *pre-trained* diffusion or flow-matching generative model to perform transition-path sampling between metastable states on atomistic energy landscapes; the reference drift is the learned score  $s_{\theta^*} \approx \nabla \log p_{\text{data}}$  of an off-the-shelf generative model and the OM action selects high-probability paths between two fixed endpoints. Our setting is complementary: we use the OM action as a *training* objective for DGP inducing-variable posterior transport (rather than a post-hoc inference criterion on a frozen model), the reference drift is the closed-form Doob-bridge PF-ODE (rather than a learned score), and the data term is an endpoint Bayesian likelihood (rather than fixed endpoints). The methodological commonality — OM action as a tractable, trace-free, low-variance path objective — is the same; the formulations apply to different problems.

**Flow matching.** Lipman et al. (2023); Liu et al. (2023); Albergo & Vanden-Eijnden (2023) developed flow matching as a deterministic alternative to score-based diffusion; Frans et al. (2025) introduced shortcut models for few-step inference. Beyond generative modelling, flow matching has been applied to probabilistic samplers (Yoon & Lee, 2024). Our work is, to our knowledge, the first application of probability-flow-ODE posterior transport to hierarchical Gaussian processes.

## 6 CONCLUSION AND LIMITATIONS

We presented **FBVI-bridge-Path**, a deterministic-ODE posterior-transport method for Deep Gaussian Processes. The construction has two ingredients: Song’s probability flow ODE applied to DBVI’s Doob-bridged forward SDE gives a closed-form reference drift; the Onsager–Machlup action provides a trace-free path-space objective. At the trained  $\alpha = 1$  ( $\epsilon = 1$ ),  $\mathcal{L}_{\text{OM}}$  is the negative log unnormalised density of an Ikeda–Watanabe finite- $\epsilon$  path posterior on  $\mathcal{C}([\delta, 1]; \mathbb{R}^M)$  — a Gaussian reference path measure tilted by the endpoint likelihood — and the inducing-variable marginal at  $\tau = 1$  retains  $\mathcal{O}(\epsilon^2)$  posterior uncertainty, which is what downstream BO and heteroscedastic-uncertainty applications consume. Theorem 1 additionally identifies  $\mathcal{L}_{\text{OM}}$  with the same posterior’s small-noise MAP path in the  $\epsilon \rightarrow 0$  Freidlin–Wentzell limit, providing the LDP mathematical anchor for the path-prior regulariser without being the regime we optimise in. The framing is rigorous, but is path-space posterior density rather than ELBO. Under matched-seed paired Wilcoxon testing on the seven UCI regression benchmarks (Appendix Q), the MAP estimator delivers statistically significant wins over DBVI on the two largest datasets — *power* ( $p = 0.014$ ) and *protein* ( $p = 0.002$ )

— statistical ties on *yacht* and *qsar*, and concedes the small- $N$  noisy datasets (*boston / energy / concrete*) to DBVI’s SDE-noise regularisation. On the same backbone, the trace-free closed-form drift dominates two strict-ELBO variants (FFJORD CNF, OM-regularised CNFOM) on every UCI cell — demonstrating that Hutchinson-trace variance, not bound looseness, is the binding constraint in this regime.

**Limitations and future work.** (i) **Not an ELBO.** The MAP framing of Theorem 1 is a rigorous large-deviation result but does not provide a lower bound on  $\log p(\mathbf{y} \mid \mathbf{x})$ . Strict-ELBO bridge variants (CNF, CNFOM, NFS<sup>2</sup>-style PINN) are available on the same backbone but empirically lose to MAP due to Hutchinson-trace MC variance; closing the gap with a low-variance strict ELBO is open. (ii) **Classification margins are tight.** On SUSY and HIGGS (Section 4.4, Table 5), FBVI-bridge-Path is in the within- $1\sigma$  tied-best group alongside DBVI on every metric (e.g. HIGGS AUC 0.807 vs. DBVI’s 0.804), but the margins are small enough that we read them as ties rather than a clear MAP win; a matched-seed paired test on the classification cells is left to future work. The image-classification benchmarks (FMNIST / CIFAR-10 / CIFAR-100) similarly show tied error rates and a substantial NLL improvement, the latter partly driven by tail-loss stabilisation rather than uniform calibration (Remark in Appendix E). (iii) **Scale.** Our largest dataset is 515k rows; scaling to the original 6M-row airline subset would strengthen the large-data case. (iv) **Few-step inference.** We have not yet exploited the determinism of FBVI-bridge-Path for consistency-model or shortcut-model few-step inference, which is a natural avenue.

**Reproducibility.** Every number in this paper is produced by a single file `fbvi_native.py` ( $\sim 1,400$  LOC, no GPyTorch dependency) and an aggregation script `aggregate_table.py`. Both will be released anonymously upon submission.

## REFERENCES

- Michael Samuel Albergo and Eric Vanden-Eijnden. Building normalizing flows with stochastic interpolants. In *The Eleventh International Conference on Learning Representations, 2023*. URL <https://openreview.net/forum?id=li7qeBbCR1t>.
- Mireille Capitaine. Onsager–machlup functional for some smooth norms on Wiener space. *Probability Theory and Related Fields*, 102(2):189–201, 1995.
- Ricky TQ Chen, Yulia Rubanova, Jesse Bettencourt, and David K Duvenaud. Neural ordinary differential equations. *Advances in neural information processing systems*, 31, 2018.
- Wuhao Chen, Zijing Ou, and Yingzhen Li. Neural flow samplers with shortcut models. In *Frontiers in Probabilistic Inference: Learning meets Sampling, 2025*.
- Andreas Damianou and Neil D Lawrence. Deep gaussian processes. In *Artificial intelligence and statistics*, pp. 207–215. PMLR, 2013.
- Amir Dembo and Ofer Zeitouni. *Large Deviations Techniques and Applications*, volume 38 of *Stochastic Modelling and Applied Probability*. Springer, 2 edition, 2010.
- Detlef Dürr and Alexander Bach. The Onsager–Machlup function as lagrangian for the most probable path of a diffusion process. *Communications in Mathematical Physics*, 60(2):153–170, 1978.
- Kevin Frans, Danijar Hafner, Sergey Levine, and Pieter Abbeel. One step diffusion via shortcut models. In *International Conference on Learning Representations*, volume 2025, pp. 34668–34684, 2025.
- Mark Iosifovich Freidlin and Alexander D Wentzell. Random perturbations. In *Random perturbations of dynamical systems*, pp. 15–43. Springer, 1998.
- Marton Havasi, José Miguel Hernández-Lobato, and Juan José Murillo-Fuentes. Inference in deep gaussian processes using stochastic gradient hamiltonian monte carlo. *Advances in neural information processing systems*, 31, 2018.
- Nobuyuki Ikeda and Shinzo Watanabe. *Stochastic Differential Equations and Diffusion Processes*, volume 24 of *North-Holland Mathematical Library*. North-Holland/Kodansha, 2 edition, 1989.

- Hilbert J Kappen. Path integrals and symmetry breaking for optimal control theory. *Journal of statistical mechanics: theory and experiment*, 2005(11):P11011–P11011, 2005.
- Minkyu Kim, Kiyoun Seong, Dongyeop Woo, Sungsoo Ahn, and Minsu Kim. On scalable and efficient training of diffusion samplers. *Advances in Neural Information Processing Systems*, 38: 26042–26068, 2026.
- Remo Kretschmann. Are minimizers of the Onsager–Machlup functional strong posterior modes? *SIAM/ASA Journal on Uncertainty Quantification*, 11(4):1105–1138, 2023.
- Christian Léonard. A survey of the schrödinger problem and some of its connections with optimal transport. *arXiv preprint arXiv:1308.0215*, 2013.
- Yaron Lipman, Ricky TQ Chen, Heli Ben-Hamu, Maximilian Nickel, and Matthew Le. Flow matching for generative modeling. In *The Eleventh International Conference on Learning Representations*, 2023.
- Xingchao Liu, Chengyue Gong, et al. Flow straight and fast: Learning to generate and transfer data with rectified flow. In *The Eleventh International Conference on Learning Representations*, 2023.
- Sanjeev Raja, Martin Šípka, Michael Psenka, Tobias Kreiman, Michal Pavelka, and Aditi S Krishnapriyan. Action-minimization meets generative modeling: Efficient transition path sampling with the Onsager–Machlup functional. *arXiv preprint arXiv:2504.18506*, 2025.
- Hugh Salimbeni and Marc Deisenroth. Doubly stochastic variational inference for deep gaussian processes. *Advances in neural information processing systems*, 30, 2017.
- Yang Song, Jascha Sohl-Dickstein, Diederik P Kingma, Abhishek Kumar, Stefano Ermon, and Ben Poole. Score-based generative modeling through stochastic differential equations. In *International Conference on Learning Representations*, 2021.
- Francisco Vargas, Will Sussman Grathwohl, and Arnaud Doucet. Denoising diffusion samplers. In *The Eleventh International Conference on Learning Representations*, 2023.
- Jian Xu, Delu Zeng, and John Paisley. Sparse inducing points in deep gaussian processes: Enhancing modeling with denoising diffusion variational inference. In *International Conference on Machine Learning*, pp. 55490–55500. PMLR, 2024.
- JIAN XU, Delu Zeng, Qibin Zhao, and John Paisley. Diffusion bridge variational inference for deep gaussian processes. In *The Fourteenth International Conference on Learning Representations*, 2026. URL <https://openreview.net/forum?id=zyRmy0Ch9a>.
- Jongmin Yoon and Juho Lee. Sequential flow straightening for generative modeling. *arXiv preprint arXiv:2402.06461*, 2024.
- Haibin Yu, Yizhou Chen, Bryan Kian Hsiang Low, Patrick Jaillet, and Zhongxiang Dai. Implicit posterior variational inference for deep gaussian processes. *Advances in neural information processing systems*, 32, 2019.
- Dinghuai Zhang, Ricky TQ Chen, Chenghao Liu, Aaron Courville, and Yoshua Bengio. Diffusion generative flow samplers: Improving learning signals through partial trajectory optimization. In *International Conference on Learning Representations*, volume 2024, pp. 47211–47232, 2024.
- Qinsheng Zhang and Yongxin Chen. Path integral sampler: A stochastic control approach for sampling. In *International Conference on Learning Representations*, 2022.

## A DETAILED SETUP: DGP, DDVI, DBVI, AND THE MOVE FROM SDE TO ODE

This appendix provides a self-contained walk-through suitable for readers familiar with DSVI (Salimbeni & Deisenroth, 2017) but new to score- or flow-based VI for DGPs. We summarise DDVI and DBVI in our notation, then explain the SDE  $\rightarrow$  probability-flow-ODE reduction that takes us from DBVI to FBVI-bridge-Path.

**DGP and sparse VI (review).** An  $L$ -layer DGP composes  $L$  Gaussian-process layers  $\mathbf{f}^{(\ell)} \sim \mathcal{GP}(0, k^{(\ell)})$  with sparse inducing variables  $\mathbf{U}^{(\ell)} \in \mathbb{R}^{M \times d_\ell}$  at locations  $\mathbf{Z}^{(\ell)}$ . The variational ELBO (single layer, multi-layer extends trivially) is

$$\mathcal{L}(\theta, \phi) = \mathbb{E}_{q_\phi(\mathbf{U})} [\log p(\mathbf{y} | \mathbf{F}^{(L)})] - D_{\text{KL}}(q_\phi(\mathbf{U}) \| p(\mathbf{U})),$$

where  $p(\mathbf{U}^{(\ell)}) = \mathcal{N}(0, K_{\mathbf{ZZ}}^{(\ell)})$  is the GP prior and  $q_\phi(\mathbf{U})$  is the variational approximation. DSVI sets  $q_\phi = \prod_\ell \mathcal{N}(m_\ell, L_\ell L_\ell^\top)$  Gaussian with analytic KL; DDVI and DBVI replace this by implicit non-Gaussian families.

**DDVI (Xu et al., 2024).** DDVI defines  $q_\phi(\mathbf{U})$  as the terminal of a *reverse-time variance-preserving SDE*:

$$dU_t = [f(t)U_t - g(t)^2 s_\phi(U_t, t)] dt + g(t) d\bar{W}_t, \quad U_T \sim \mathcal{N}(0, \sigma^2 I), \quad U_0 \sim q_\phi.$$

The score  $s_\phi$  is a neural network trained to approximate  $\nabla_U \log p_t(U)$  via denoising score matching (DSM) against the forward VP-SDE marginals. The ELBO is derived via Girsanov, giving an  $\int_0^1 g(t)^2 \|s_\phi - \text{score}\|^2 dt$  penalty plus the data term. The base distribution  $\mathcal{N}(0, \sigma^2 I)$  is data-agnostic, so sampling has to traverse the full distance from noise to posterior.

**DBVI (XU et al., 2026).** DBVI fixes DDVI’s data-agnostic start by amortising the initial mean:  $p_0^\theta(U_0 | \mathbf{x}) = \mathcal{N}(\mu_\theta(\mathbf{x}), \sigma_0^2 I)$ . The forward process is no longer unconstrained noising but a *Doob  $h$ -transformed bridge SDE* that ends at a fixed noise marginal:

$$dU_s = [-\lambda(s)U_s + g(s)^2 h(U_s, s, U_0)] ds + g(s) dW_s,$$

with  $h(U_s, s, U_0) = \nabla_{U_s} \log p(U_T | U_s)$  the Doob correction. The reverse-time bridge SDE is then driven by a *conditional* score  $s_\phi(U_t, t, \text{ctx})$ , trained by conditional DSM against the closed-form bridge marginal. The ELBO is again Girsanov-form, but the shorter path (the bridge is much closer to the posterior than VP noise) and the data-conditioned start yield faster, more accurate inference. We retain the same Doob bridge SDE as the *reference process* of FBVI-bridge-Path.

**Why move from SDE to ODE? (motivation for our work).** Song et al. (2021) showed that any SDE of the form  $dU_s = b(U_s, s) ds + g dW_s$  has a deterministic counterpart, the *probability flow ODE*,  $dU_s = (b - \frac{1}{2} g^2 \nabla \log p_s) ds$ , with identical marginals. The ODE is preferred whenever (i) the variational density needs closed-form evaluation, (ii) the sampler benefits from determinism (faster inference, fewer steps), or (iii) the loss can be expressed without score-matching auxiliary regression. We exploit (i) and (iii) in FBVI-bridge-Path: the closed-form reference drift comes from the SDE’s deterministic counterpart (Lemma 1), and the loss is the Onsager–Machlup action against this drift (Theorem 1), which is trace-free and avoids DSM.

## B PROOFS AND DERIVATIONS

### B.1 PROOF OF LEMMA 1

We show that the SDE  $dU_s = b ds + g dW_s$  and the ODE  $dU_s = (b - \frac{1}{2} g^2 \nabla \log p_s) ds$  share marginals  $p_s$ .

The Fokker–Planck equation of the SDE is

$$\partial_s p_s(U) = -\nabla \cdot (b p_s) + \frac{1}{2} g^2 \Delta p_s.$$

Using  $\Delta p_s = \nabla \cdot \nabla p_s = \nabla \cdot (p_s \nabla \log p_s)$  (multiply and divide by  $p_s$ ),

$$\partial_s p_s = -\nabla \cdot (b p_s) + \frac{1}{2} g^2 \nabla \cdot (p_s \nabla \log p_s) = -\nabla \cdot (p_s [b - \frac{1}{2} g^2 \nabla \log p_s]),$$

which is the continuity equation of the ODE  $dU_s = (b - \frac{1}{2} g^2 \nabla \log p_s) ds$ . Both equations therefore propagate the same density  $p_s$ .  $\square$

## B.2 PROOF OF LEMMA 2

For Gaussian  $p_s(U) = \mathcal{N}(U; m_s, \kappa_s I)$ , we have  $\nabla \log p_s(U) = -(U - m_s)/\kappa_s$ . The Fokker–Planck ODE drift for preserving this marginal is, by Lemma 1, any  $v$  such that  $\partial_s p_s + \nabla \cdot (p_s v) = 0$ . We show  $v(U, s) = \dot{m}_s + \frac{\dot{\kappa}_s}{2\kappa_s}(U - m_s)$  satisfies this: the first moment evolves as  $\mathbb{E}_{p_s}[v] = \dot{m}_s$  (the linear  $(U - m_s)$  term has zero mean), matching  $\dot{m}_s$ ; and the second central moment evolves as  $\mathbb{E}_{p_s}[(U - m_s)v] = \frac{\dot{\kappa}_s}{2\kappa_s}\kappa_s = \frac{\dot{\kappa}_s}{2}$ , giving  $\partial_s \mathbb{E}_{p_s}[(U - m_s)^2] = 2 \cdot \frac{\dot{\kappa}_s}{2} = \dot{\kappa}_s$ , matching  $\dot{\kappa}_s$ . *Uniqueness within the affine-drift class.* The Fokker–Planck equation  $\partial_s p_s + \nabla \cdot (p_s v) = 0$  does not determine  $v$  uniquely without further constraint: adding any  $w$  with  $\nabla \cdot (p_s w) = 0$  leaves the marginal-flow equation invariant (the standard non-uniqueness of probability flows). We do *not* claim uniqueness over all such  $v$ . Restricted to the *affine-in- $U$  class*  $v(U, s) = a(s) + b(s)(U - m_s)$  — the class that preserves the Gaussian structure of  $p_s$  under the affine bridge SDE — the two moment-matching equations  $\mathbb{E}_{p_s}[v] = \dot{m}_s$  and  $\mathbb{E}_{p_s}[(U - m_s)v^\top] + \mathbb{E}_{p_s}[v(U - m_s)^\top] = \dot{\kappa}_s I$  uniquely determine  $a(s) = \dot{m}_s$  and  $b(s) = \dot{\kappa}_s/(2\kappa_s)$ . The expression for  $v_{\text{ref}}^{\text{Bri}}$  used throughout the paper is therefore the unique *affine* PF-ODE drift compatible with the bridge Gaussian marginals (Lemmas 1–2); this is the natural choice given the bridge construction, but a non-affine  $v$  would produce a different (non-Gaussian) marginal flow to the same  $p_s$ .  $\square$

## B.3 PROOF OF THEOREM 1

We follow the Freidlin–Wentzell large-deviation programme (Freidlin & Wentzell, 1998, Ch. 3), working throughout on the path space  $\mathcal{C}([\delta, 1]; \mathbb{R}^M)$  with the uniform topology, with the endpoint cutoff  $\delta \in (0, 1)$  of (A1).

**Setup.** Fix the reference  $\epsilon$ -perturbed SDE in reverse-time  $\tau \in [\delta, 1]$ ,

$$dU_\tau = -v_{\text{ref}}^{\text{Bri}}(U_\tau, 1 - \tau) d\tau + \epsilon dW_\tau, \quad U_\delta \sim p_0^\epsilon, \quad (17)$$

where the initial law  $p_0^\epsilon$  is taken to be the  $\epsilon$ -rescaled Gaussian  $\mathcal{N}(\phi(1)\mu_\theta(\mathbf{Z}), \epsilon^2 \kappa(1)I)$  on  $[\delta, 1]$ ; this is the conventional choice that gives an LDP with the quadratic initial rate  $I_0(u_\delta) = \frac{1}{2}\kappa(1)^{-1}\|u_\delta - \phi(1)\mu_\theta(\mathbf{Z})\|^2$  and is compatible with the path-LDP rate-functional form below. *Mismatch with Algorithm 1 (line 4).* At training time we instead draw  $U_\delta \sim \mathcal{N}(\phi(1)\mu_\theta(\mathbf{Z}), \kappa(1)I)$ , i.e. the  $\epsilon = 1$  marginal, not the  $\epsilon$ -rescaled one. This mismatch between the FW initial distribution used in the proof and the finite- $\epsilon$  initial distribution used in Algorithm 1 is a conceptual gap; it leaves the path-integral part of the rate functional unchanged, and because the per-trajectory MAP optimisation conditions on  $u_\delta = u_0$  (so  $I_0$  becomes a path-independent constant that drops from the variational loss), the gap does not affect the final form of  $\mathcal{L}_{\text{OM}}$ . We flag this as a separate concept-vs-implementation slack, of a piece with the finite- $\alpha$  gap of Remark 2 and the  $\delta$ -cutoff gap of Remark 3. Under (A1) the drift  $-v_{\text{ref}}^{\text{Bri}}(\cdot, 1 - \tau)$  is bounded and globally Lipschitz in  $U$  on  $[\delta, 1] \times \mathbb{R}^M$ , so the Freidlin–Wentzell regularity hypothesis applies. Write the path measure as  $\mathbb{P}_{\text{ref}}^\epsilon$ . The tempered Doob-bridge path posterior is

$$\frac{d\mathbb{P}_y^\epsilon}{d\mathbb{P}_{\text{ref}}^\epsilon}(U_{\delta:1}) = \frac{1}{Z^\epsilon} p(\mathbf{y} \mid \text{dgp}(U_1))^{1/\epsilon^2}, \quad Z^\epsilon = \mathbb{E}_{\mathbb{P}_{\text{ref}}^\epsilon}[p(\mathbf{y}|U_1)^{1/\epsilon^2}],$$

a likelihood-tilt of  $\mathbb{P}_{\text{ref}}^\epsilon$  with inverse temperature  $\beta = 1/\epsilon^2$ . By (A2), the Varadhan tail condition holds, so  $Z^\epsilon$  is finite and the tilted measure  $\mathbb{P}_y^\epsilon$  is well-defined.

**Remark: divergence (Stratonovich) term.** The full classical Onsager–Machlup functional for a reference SDE  $dU = -v dt + \epsilon dW$  on  $H^1$  paths is  $\tilde{S}_{\text{OM}}(u) = \frac{1}{2} \int \|\dot{u} + v\|^2 dt + \frac{1}{2} \int \nabla \cdot v dt$  (Dürr & Bach, 1978; Ikeda & Watanabe, 1989); the second term is the Stratonovich correction arising from the change-of-measure Jacobian. In our setting  $v_{\text{ref}}^{\text{Bri}}(U, s) = \dot{\phi}(s)\mu_\theta(\mathbf{Z}) + (\dot{\kappa}(s)/(2\kappa(s)))(U - \phi(s)\mu_\theta(\mathbf{Z}))$  is *affine* in  $U$  (Lemma 2, Eq. equation 6), so its divergence is the path-independent scalar  $\nabla \cdot v_{\text{ref}}^{\text{Bri}}(U, s) = M \dot{\kappa}(s)/(2\kappa(s))$ . The Stratonovich integral  $\frac{1}{2} \int_\delta^1 M \dot{\kappa}(s)/(2\kappa(s)) ds = (M/4) \log[\kappa(1)/\kappa(\delta)]$  is therefore a path-independent constant that absorbs into the normaliser  $Z^\epsilon$  and drops out of the MAP optimisation. We omit it from  $S_{\text{OM}}$  throughout; this absorption is specific to the Gaussian-marginal / affine-drift setting and would not hold for a non-Gaussian bridge.

**Reference rate functional (LDP form).** By Freidlin–Wentzell (Freidlin & Wentzell, 1998, Theorem 3.2.1) on  $\mathcal{C}([\delta, 1]; \mathbb{R}^M)$  under the uniform topology, the family  $\{\mathbb{P}_{\text{ref}}^\epsilon\}_{\epsilon>0}$  satisfies a full LDP with good rate functional

$$I_{\text{ref}}(u) = \frac{1}{2} \int_{\delta}^1 \|\dot{u}_\tau + v_{\text{ref}}^{\text{Bri}}(u_\tau, 1 - \tau)\|^2 d\tau + I_0(u_\delta)$$

for  $u \in H^1([\delta, 1]; \mathbb{R}^M)$  (and  $+\infty$  otherwise), where  $I_0(u_\delta) = \frac{1}{2} \kappa(1)^{-1} \|u_\delta - \phi(1) \mu_\theta(\mathbf{Z})\|^2$  is the Gaussian initial rate functional (using  $p_0^\epsilon$ 's weak limit). Concretely, for any open  $O \subseteq \mathcal{C}([\delta, 1]; \mathbb{R}^M)$ ,

$$\liminf_{\epsilon \rightarrow 0} \epsilon^2 \log \mathbb{P}_{\text{ref}}^\epsilon(U \in O) \geq - \inf_{u \in O} I_{\text{ref}}(u), \quad (18)$$

with the matching closed-set upper bound; the abbreviated ‘‘pointwise’’ notation  $-\epsilon^2 \log \mathbb{P}_{\text{ref}}^\epsilon\{U \approx u\} = I_{\text{ref}}(u) + o(1)$  used in the main text is shorthand for the shrinking-tubular-neighbourhood limit guaranteed by (A3).

**Tempered posterior rate functional.** Applying Varadhan’s lemma (Dembo & Zeitouni, 2010, Theorem 4.3.1) to the tilt  $p(\mathbf{y}|U_1)^{1/\epsilon^2}$  — which is justified by the tail condition in (A2) and the continuity of  $U \mapsto -\log p(\mathbf{y}|U_1)$  in the uniform topology (it depends only on the endpoint  $U_1$ ) — the free energy converges to

$$-\epsilon^2 \log Z^\epsilon \xrightarrow{\epsilon \rightarrow 0} \inf_{u \in H^1} \{ -\log p(\mathbf{y}|u_1) + I_{\text{ref}}(u) \}.$$

The contraction principle then yields the LDP for  $\{\mathbb{P}_y^\epsilon\}$  with rate functional

$$I_y(u) = -\log p(\mathbf{y} | u_1) + I_{\text{ref}}(u) - \inf_{u' \in H^1} I_y(u'), \quad (19)$$

where the infimum subtraction enforces  $\inf I_y = 0$  (a normalisation constant absorbed into  $Z^\epsilon$ ). The likelihood enters with weight 1 (not  $1/\epsilon^2$ ) because the tempering  $\beta = 1/\epsilon^2$  was chosen exactly so that the data-tilt and the reference rate remain  $\mathcal{O}(1)$  in the  $\epsilon^2 \log$  scale.

**MAP path (per- $u_0$ ).** For each initial point  $u_\delta = u_0 \in \mathbb{R}^M$ , restrict  $I_y$  to paths satisfying  $u_\delta = u_0$ ; the conditional MAP path is

$$u^*(u_0) = \arg \min_{\substack{u \in H^1([\delta, 1]; \mathbb{R}^M) \\ u_\delta = u_0}} \left\{ -\log p(\mathbf{y} | u_1) + \underbrace{\frac{1}{2} \int_{\delta}^1 \|\dot{u}_\tau + v_{\text{ref}}^{\text{Bri}}(u_\tau, 1 - \tau)\|^2 d\tau}_{S_{\text{OM}}(u; v_{\text{ref}}^{\text{Bri}})} \right\},$$

the  $I_0(u_0)$  term being constant under the  $u_\delta = u_0$  restriction. This proves equation 10.

**Restriction to ODE-parameterised paths (amortisation).** The unconstrained per- $u_0$  MAP  $\{u^*(u_0)\}_{u_0}$  is a family in  $H^1([\delta, 1]; \mathbb{R}^M)$ . We restrict the search to ODE-parameterised paths  $u^{v_\phi}$  generated by  $\dot{u}_\tau = v_\phi(u_\tau, 1 - \tau, \text{ctx})$  with  $u_\delta \sim p_0^\epsilon$ , and seek the single  $\phi$  that minimises the  $u_0$ -expectation of the per-trajectory MAP objective:

$$\phi^* = \arg \min_{\phi} \mathbb{E}_{u_0} \left[ \mathcal{J}(u^{v_\phi}; u_0) \right], \quad \mathcal{J}(u; u_0) = -\log p(\mathbf{y}|u_1) + S_{\text{OM}}(u; v_{\text{ref}}^{\text{Bri}}).$$

This is an amortisation step: a single  $v_\phi$  approximates the family  $\{u^*(u_0)\}_{u_0}$  jointly. It is a *modelling choice*, not a theorem consequence — the amortised optimum is in general weaker than the per- $u_0$  MAP family, with equality only when  $\{u^*(u_0)\}_{u_0}$  lies inside the ODE-parameterised submanifold. Substituting the ODE trajectory and pushing the expectation through the integrals, the boundary term  $I_0(u_\delta)$  integrates against  $u_\delta \sim p_0^\epsilon$  to a constant ( $\frac{1}{2}M$  in the Gaussian limit) independent of  $\phi$  that we drop, and we absorb the  $\delta \downarrow 0^+$  endpoint contribution into  $o(1)$  by (A1). This gives

$$\mathcal{L}_{\text{OM}}(\theta, \phi) = -\mathbb{E}_{q_\phi}[\log p(\mathbf{y} | \mathbf{F}^{(L)})] + \frac{\alpha}{2} \int_0^1 \mathbb{E}[\|v_\phi - v_{\text{ref}}^{\text{Bri}}\|^2] d\tau + \text{const},$$

where we have reintroduced  $\alpha = 1/\epsilon^2$  in front of  $S_{\text{OM}}$  to make the inverse-temperature dependence explicit. Theorem 1 corresponds to  $\alpha \rightarrow \infty$ ; the practical  $\alpha = 1$  regime is treated as a hyperparameter (Remark 2, Appendix O). Dropping the constant yields Eq. equation 12.

**What the theorem does—and does not—establish.** Eq. equation 12 is a rigorous identification of  $\mathcal{L}_{\text{OM}}$  with the small-noise MAP path estimator of the tempered Doob-bridge path posterior  $\mathbb{P}_y^e$ . It is not a variational lower bound on  $\log p(\mathbf{y} | \mathbf{x})$ : the data marginal would require either an endpoint-density log-det term (FFJORD/CNF, Section 3.4) or a path-space Girsanov KL (DBVI), neither of which appears here. Strict ELBO posterior-transport variants on the same backbone are reported in Section 3.4 and Appendix H.  $\square$

#### B.4 PROOF OF PROPOSITION 1

The Doob  $h$ -transformed bridge is the SDE that propagates the joint distribution  $p_0^\theta \otimes p_1^{\text{fix}}$  along the affine OU prior; its forward drift acquires an additive  $h$ -correction. Concretely (XU et al., 2026, §2), the bridge SDE in forward-bridge time  $s$  is

$$dU_s = [-\lambda U_s + g^2 \nabla_{U_s} \log p_1^{\text{fix}}(U_s)] ds + g dW_s,$$

where the score of the terminal marginal under the OU transition is  $\nabla_{U_s} \log p_1^{\text{fix}}(U_s) = c_s (a_s U_0 - U_s) / q_s$  with  $a_s, q_s, c_s$  as in Prop. 1. Under Gaussian initial and Gaussian terminal, the marginal at each  $s$  is also Gaussian; write  $p_s^{\text{Bri}}(U_s | \mathbf{x}) = \mathcal{N}(m_s, \kappa_s I)$ . Substituting the Gaussian ansatz into the forward Kolmogorov (Fokker–Planck) equation and matching the first and second moments gives the ODE system equation 15–equation 16: the drift contributes  $\dot{m}_s = -(\lambda + c_s)m_s + c_s a_s \mu_\theta(\mathbf{x})$ , and the second-moment balance gives the  $\kappa$  equation. The boundary values  $\phi(0) = 1$ ,  $\kappa(0) = \sigma_0^2$  encode the anchored start as one-sided limits enforced by the initial distribution  $p_0^\theta(U_0 | \mathbf{x}) = \mathcal{N}(\mu_\theta(\mathbf{x}), \sigma_0^2 I)$ . The coefficient  $c_s = g^2 \sigma_0^2 a_s^2 / [(a_s^2 \sigma_0^2 + q_s) q_s]$  diverges as  $s \downarrow 0^+$  because  $q_s \sim g^2 s \rightarrow 0$ , yielding  $c_s \sim 1/s$  near the anchor (the standard Doob  $h$ -transform conditioning singularity). The system equation 15–equation 16 is regular on the open interval  $s \in (0, 1]$ , and our LDP analysis (Appendix B.3) works on the truncated interval  $[\delta, 1]$  where  $c_s \leq c_\delta < \infty$ .  $\square$

#### B.5 PROOF OF PROPOSITION 2

We compare trace covariances at the FBVI / FBVI-bridge initial distributions.

- FBVI:  $U_0 \sim \mathcal{N}(0, K_{\mathbf{ZZ}})$ , so  $\text{tr}_{\text{FBVI}} = \text{tr}(K_{\mathbf{ZZ}}) = \sum_{m=1}^M K(z_m, z_m)$ .
- FBVI-bridge:  $U_0 \sim \mathcal{N}(\phi(1)\mu_\theta(\mathbf{x}), \kappa(1)I_M)$  (isotropic by Prop. 1), so  $\text{tr}_{\text{bridge}} = M \kappa(1)$ .

For our default hyperparameters  $\lambda = g = \sigma_0 = 1$ , numerical Euler integration of Eq. equation 16 with a 100-point grid gives  $\kappa(1) \approx 0.50$  and  $\phi(1) \approx 0.37$ . Meanwhile  $K_{\mathbf{ZZ}}$  uses an ARD-RBF kernel with unit amplitude at initialisation ( $\log \sigma_k = 0$ ); diagonal entries equal 1, so  $\text{tr}(K_{\mathbf{ZZ}}) = M$ , giving  $\text{tr}_{\text{FBVI}}/M = 1$  versus  $\text{tr}_{\text{bridge}}/M = \kappa(1) \approx 0.50$ , i.e. the bridge initial variance per coordinate is approximately half of FBVI’s. We verified this by running `_precompute_doob` in our code with  $n_{\text{grid}} = 100$  and the above parameters, obtaining  $\phi(1) = 0.367$ ,  $\kappa(1) = 0.504$ . For larger  $\lambda$  the gap widens (e.g.  $\lambda = 2$ :  $\kappa(1) = 0.250$ ,  $\phi(1) = 0.134$ ).  $\square$

#### B.6 PROOF OF PROPOSITION 3

The DBVI bridge SDE is

$$dU_t = b_{\text{Bri}}(U_t, t, U_0) dt + g(t) dW_t, \quad b_{\text{Bri}}(U, t, U_0) = -\lambda U + g(t)^2 h(U, t, U_0),$$

with conditional bridge score  $h(U, t, U_0) = \nabla_U \log p_t^{\text{Bri}}(U | U_0)$ . By Song’s identity (Song et al., 2021, Theorem 1) (our Lemma 1), the time- $t$  marginal of this SDE equals the marginal of the deterministic probability-flow ODE

$$\dot{U}_t = b_{\text{Bri}}(U_t, t, U_0) - \frac{1}{2} g(t)^2 \nabla_U \log p_t^{\text{Bri}}(U_t),$$

which under the Gaussian bridge marginal (Prop. 1) has the closed form  $-v_{\text{ref}}^{\text{Bri}}(U_t, t)$  derived in Lemma 2. The FBVI-bridge ODE  $\dot{U}_\tau = v_\phi(U_\tau, 1 - \tau, \text{ctx})$  parameterises this PF-ODE drift by a free neural velocity in reverse time. At the population optimum  $v_\phi \equiv v_{\text{ref}}^{\text{Bri}}$ , FBVI-bridge has the same time- $t$  marginals as DBVI’s bridge SDE (claim (i)). Because  $v_\phi$  has no factorisation constraint, it can express drifts outside the  $-\lambda U + g^2 h - \frac{1}{2} g^2 \nabla \log p$  family — for instance, drifts trained

directly against an OM action rather than via DSM matching of  $h$  — so FBVI-bridge is strictly more expressive than the DBVI bridge SDE (claim (ii)).

*What this proposition does not say.* A formal  $g(t) \rightarrow 0$  limit of the bridge SDE would set both the Brownian term and the score correction  $g^2 h$  to zero (the latter because  $h$  remains bounded in our Gaussian-bridge setting while  $g^2 \rightarrow 0$ ), leaving the unconditional OU flow  $\dot{U}_t = -\lambda U_t$ , which obviously cannot match a data-conditioned posterior. The relation between DBVI and FBVI-bridge is *not* a vanishing-diffusion limit — it is the deterministic probability-flow ODE associated with the same SDE, which retains the score correction in transmuted form (the  $-\frac{1}{2}g^2 \nabla \log p_t$  term).  $\square$

## B.7 PROOF OF PROPOSITION 4

Let  $f(U, \tau) = v_\phi(U, 1 - \tau, \text{ctx})$  denote the ODE right-hand side in  $\tau$ . Under the stated Lipschitz conditions,

$$\|f(U, \tau) - f(U', \tau')\| \leq L_v \|U - U'\| + L_s |\tau - \tau'|.$$

The standard Grönwall–Euler recursion for global error is, with stepsize  $h=1/N$  and per-step local truncation  $T \leq \frac{1}{2}h^2 \sup_\tau \|f'\|$ ,

$$\|U_{k+1}^{(N)} - U_{k+1}^{(\infty)}\| \leq (1 + hL_v) \|U_k^{(N)} - U_k^{(\infty)}\| + T.$$

Iterating this recursion from  $k=0$  ( $\|U_0^{(N)} - U_0^{(\infty)}\| = 0$ ) gives the closed-form bound

$$\|U_N^{(N)} - U_N^{(\infty)}\| \leq T \sum_{k=0}^{N-1} (1 + hL_v)^k = T \frac{(1 + hL_v)^N - 1}{hL_v} \leq \frac{T(e^{L_v} - 1)}{hL_v} = \mathcal{O}(h).$$

This is the standard  $\mathcal{O}(h) = \mathcal{O}(1/N)$  global Euler rate in  $\|\cdot\|$  (each of the  $N$  steps contributes  $\mathcal{O}(h^2)$  local error, accumulating to  $N \cdot h^2 = h$ ). The chain-rule bound  $\|f'\| \leq L_v \|f\| + L_s$  then gives  $T \leq \frac{h^2}{2}(L_v \|f\| + L_s)$ . Squaring and taking expectation:

$$\mathbb{E}\|U_N^{(N)} - U_N^{(\infty)}\|^2 \leq \left[\frac{e^{L_v} - 1}{L_v}\right]^2 \frac{h^2}{4} (L_v^2 \mathbb{E}\|f\|^2 + L_s^2) = \mathcal{O}(h^2) = \mathcal{O}(1/N^2).$$

This is the squared-error variant we report (the  $\mathcal{O}(1/N^2)$  rate is the well-known Euler-method  $L^2$  rate). Using  $\mathbb{E}\|U_0\|^2 = \kappa(1)$  (Prop. 1) and Grönwall propagation of  $\|f\|^2 \leq 2L_v^2 \sup_\tau \|U_\tau\|^2 + 2L_s^2$  along the trajectory yields  $\mathbb{E}\sup_\tau \|U_\tau\|^2 \leq e^{2L_v} \kappa(1)$ . Collecting numerical constants into  $C_v$  gives the stated bound.  $\square$

## B.8 KL TERM AND ITS SAMPLE-BASED SURROGATE

We adopt the implicit- $q$  treatment of Xu et al. (2024). The exact KL is

$$D_{\text{KL}}(q_\phi \| p) = \mathbb{E}_{q_\phi} [\log q_\phi(\mathbf{U}) - \log p(\mathbf{U})].$$

The second term is the Gaussian-prior log-density which is tractable; the first term requires either the (intractable) implicit-flow Jacobian determinant or a sample-based surrogate. We use a surrogate that drops the  $\log q_\phi$  contribution and corrects via a KL anneal: in our setup we multiply the prior log-likelihood by  $\beta_t \in [0, 1]$  that ramps from  $10^{-3}$  at  $t = 0$  to 1 over the first 20 epochs. This is the same treatment used in DDVI/DBVI and is justified empirically: dropping the  $\log q_\phi$  term introduces a bias proportional to the differential entropy of  $q_\phi$ , which is bounded above by the prior entropy and below by zero for our parameterisation. The bias has the same sign for all methods compared and does not affect cross-method ranking.

## C FM AUXILIARY-LOSS ABLATION

We ablate adding an annealed-Langevin flow-matching regression loss  $\mathcal{L}_{\text{FM}} = \mathbb{E}_{t, U_t} \|v_\phi(U_t, t, \text{ctx}) - \nabla \log \pi_t(U_t)\|^2$  to FBVI-bridge with weight  $\lambda \in \{0, 10^{-3}, 10^{-2}, 10^{-1}, 1\}$ . With  $\lambda \leq 10^{-3}$  results are statistically indistinguishable from the no-FM baseline; with  $\lambda \geq 10^{-2}$  test NLL degrades by 10–30%. The ELBO data term already supplies sufficient training signal through the integrator.

## D FFJORD ABLATION: EXPLICIT VS IMPLICIT $q$

To justify the implicit- $q$  design we ablate against an explicit continuous normalising flow with Hutchinson-trace divergence (FFJORD-style). The FFJORD variant integrates the ODE while accumulating  $\int_0^1 \text{tr}(\partial v / \partial U) dt$  via Hutchinson’s estimator, so that  $\log q(U_1) = \log q(U_0) - \int_0^1 \text{div } v$  is available in closed form and the KL term in the ELBO can be evaluated exactly. All other components (sparse-GP backbone, MC budget, optimiser, seeds) are identical. Table A1 and Table A2 report results on the seven small/medium datasets. The implicit- $q$  variants (FBVI, FBVI-bridge) dominate the explicit-Jacobian variant on 6/7 datasets for both RMSE and NLL; only on *qsar* are the three approaches statistically tied. Two factors plausibly contribute: (i) the Hutchinson trace introduces extra Monte-Carlo noise into the ELBO gradient; (ii) the explicit  $\log q$  couples the divergence and the data terms more tightly, making optimisation harder.

Table A1: FFJORD ablation: test RMSE on small/medium UCI ( $L = 2, 5$  seeds). **Bold** = tied-best group.

Method	yacht	boston	energy	qsar	concrete	power	protein
FBVI	<b>.239±.024</b>	<b>.371±.053</b>	<b>.167±.015</b>	<b>.648±.052</b>	<b>.404±.037</b>	<b>.255±.006</b>	.831±.007
FBVI-br (impl- $q$ )	<b>.216±.031</b>	<b>.370±.057</b>	<b>.167±.013</b>	<b>.648±.045</b>	<b>.390±.040</b>	<b>.255±.008</b>	.827±.010
FBVI-CNF (FFJORD)	.380±.057	.480±.056	.291±.029	<b>.647±.058</b>	.477±.039	.280±.017	.852±.007
<b>FBVI-br-Path (OM)</b>	.245±.016	.426±.031	.227±.029	<b>.680±.039</b>	.433±.039	<b>.247±.004</b>	<b>.745±.008</b>

Table A2: FFJORD ablation: test NLL.

Method	yacht	boston	energy	qsar	concrete	power	protein
FBVI	.549±.016	<b>.640±.060</b>	.494±.012	<b>1.014±.060</b>	<b>.675±.036</b>	.309±.019	1.239±.007
FBVI-br (impl- $q$ )	.526±.020	<b>.635±.063</b>	.491±.009	<b>1.014±.055</b>	<b>.656±.039</b>	.308±.029	1.235±.010
FBVI-CNF (FFJORD)	.775±.031	.845±.057	.623±.012	1.045±.060	.862±.032	.473±.014	1.266±.008
<b>FBVI-br-Path (OM)</b>	<b>.606±.001</b>	.736±.030	<b>.567±.021</b>	<b>1.033±.048</b>	.739±.031	<b>.022±.014</b>	<b>1.128±.008</b>

## E IMAGE CLASSIFICATION BENCHMARKS

We test the framework on three standard image-classification benchmarks following the now-standard “frozen-feature + Bayesian head” recipe:

1. Resize each image to  $224 \times 224$  and apply the standard ImageNet mean/std normalisation (Fashion-MNIST is replicated from grayscale to 3 channels for ResNet compatibility).
2. Forward through an ImageNet-pretrained ResNet-50 (IMAGENET1K\_V2 weights, 80.86% ImageNet top-1) with the final classification head removed, yielding a 2048-dimensional penultimate feature per image; this is done once and cached.
3. Train a 2-layer DGP head ( $M = 128$  inducing, hidden width 64) end-to-end on the cached features with each of the four VI methods (DSVI, DBVI, FBVI, FBVI-bridge),  $T = 50$  epochs, Adam at  $10^{-2}$ , batch size 1024.

The feature extractor is identical across methods, so this experiment isolates the contribution of the variational head. We use the same ResNet-50 V2 weights across all runs.

Table A3 reports test error and NLL on FMNIST, CIFAR-10, and CIFAR-100. Three observations:

- **Top-1 accuracies cluster in the same band across methods** (FMNIST 87.8%–88.1%, CIFAR-10 88.6%–88.8%, CIFAR-100 64.6%–68.0%), broadly consistent with typical ResNet-50 + DGP-head numbers in the literature. The remaining gap is consistent with our deliberately conservative head budget (2 GP layers,  $M = 128$ , hidden 64) and a fully frozen feature extractor.
- **On error rate, all density-VI methods are within one standard deviation on FMNIST and CIFAR-10; FBVI-bridge-Path is 3.4 percentage points worse on CIFAR-100** (0.354 vs 0.320). The 100-way softmax with a 2-layer DGP head is harder to fit with

a deterministic posterior sampler at the same budget—consistent with the small/noisy data pattern observed elsewhere in the paper.

- **On NLL, however, FBVI-bridge-Path is dramatically better on all three datasets** (FMNIST 0.680 vs  $\geq 0.814$  for the others; CIFAR-10 1.640 vs  $\geq 1.945$ ; CIFAR-100 **7.009** vs  $\geq 13.910$ , roughly half the NLL). Two non-exclusive mechanisms contribute, and we list both to avoid overclaiming. (i) *Calibration*. The density-VI baselines make confident wrong predictions: their posterior concentrates around the MLE mode and predicted probabilities saturate near 0/1, so cross-entropy at mis-classified samples is large. FBVI-bridge-Path’s Doob-bridge path prior keeps the inducing posterior more spread out, so wrong predictions retain non-trivial mass on the true class. (ii) *Numerical stability of NLL*. Cross-entropy penalises predicted probability  $p \rightarrow 0$  as  $\log(1/p)$ , which is essentially unbounded on the rare hardest examples. A small fraction of samples on CIFAR-100 with  $p_{\text{true}} \approx 10^{-6}$  already contributes NLL  $\sim 14$  per sample, so a few tail samples can dominate the mean. The wider OM-Path posterior caps the worst-case per-sample contribution, recovering a substantial NLL gap that is partly a tail-loss stabilisation effect rather than a uniform calibration improvement. Consistent with the latter, the ECE numbers in Appendix L (Table A8) show OM-Path roughly tied with DSVI on CIFAR-100 (0.2917 vs. 0.2938), i.e. the average-calibration improvement is small even though the mean NLL drops by a factor of two. We read this as: the path prior helps both across-the-distribution calibration (modestly) and tail-event NLL stability (substantially), with the NLL halving on CIFAR-100 dominated by the latter.

Table A3: Image classification: ImageNet-pretrained ResNet-50 V2 (2048-d, 80.86% ImageNet top-1) frozen features followed by a 2-layer DGP head ( $M = 128$  inducing, hidden 64),  $T = 50$  epochs. Mean $\pm$ std over 2 seeds. **Bold** = tied-best per column (within 1 std).

Method	FMNIST		CIFAR-10		CIFAR-100	
	Err $\downarrow$	NLL $\downarrow$	Err $\downarrow$	NLL $\downarrow$	Err $\downarrow$	NLL $\downarrow$
DSVI	<b>0.120<math>\pm</math>0.001</b>	<b>0.814<math>\pm</math>0.016</b>	<b>0.114<math>\pm</math>0.003</b>	<b>1.945<math>\pm</math>0.083</b>	0.326 $\pm$ 0.001	14.214 $\pm$ 0.015
DBVI	<b>0.120<math>\pm</math>0.001</b>	0.845 $\pm$ 0.001	<b>0.112<math>\pm</math>0.001</b>	1.999 $\pm$ 0.015	0.321 $\pm$ 0.001	14.118 $\pm$ 0.030
FBVI	<b>0.119<math>\pm</math>0.001</b>	<b>0.825<math>\pm</math>0.012</b>	<b>0.113<math>\pm</math>0.002</b>	2.031 $\pm$ 0.007	0.320 $\pm$ 0.001	<b>13.910<math>\pm</math>0.219</b>
FBVI-br (impl- $q$ )	<b>0.121<math>\pm</math>0.003</b>	0.839 $\pm$ 0.007	<b>0.113<math>\pm</math>0.001</b>	2.027 $\pm$ 0.028	0.320 $\pm$ 0.000	13.927 $\pm$ 0.008
<b>FBVI-br-Path (OM)</b>	<b>0.122<math>\pm</math>0.001</b>	<b>0.680<math>\pm</math>0.022</b>	<b>0.114<math>\pm</math>0.000</b>	<b>1.640<math>\pm</math>0.007</b>	0.354 $\pm$ 0.000	<b>7.009<math>\pm</math>0.093</b>

## F ADVERSARIAL STABILITY DISCUSSION

In our framework the IPVI generator–discriminator pair requires several implementation tricks to reach the performance reported in the original paper. The most important are: parameter tying within the inducing layer (Section 4 of Yu et al.), separate learning rates for generator and discriminator (typically 5–10 $\times$  ratio), and an entropy-stabilising warmup. Even with these, seed-level NLL standard deviation on small datasets remains 5–10 $\times$  that of non-adversarial methods. We view this as a property of the adversarial VI family rather than of IPVI specifically. Our recommendation is that adversarial DGP-VI should be reserved for settings where the additional model flexibility is empirically necessary.

## G CLASSIFICATION PRECISION AND RECALL

Table A4 reports per-method precision and recall on SUSY and HIGGS. The pattern is the diagnostic for IPVI’s collapse: recall  $\approx 1$  with precision near the class prior means the discriminator stopped distinguishing classes and the generator settled on the all-positive prediction. DDVI’s seed-to-seed variability is reduced (but not eliminated) by the logit-clip + tighter-grad-clip protocol described in Section 4.4. The non-degenerate methods (DSVI, SGHMC, DBVI, FBVI-bridge) sit in a tight cluster on precision (0.82–0.85 SUSY, 0.70–0.73 HIGGS) and recall (0.68–0.77).

Table A4: Binary classification: precision and recall (3 seeds). **Bold** = tied-best per column.

Method	SUSY		HIGGS	
	Precision	Recall	Precision	Recall
DSVI	0.824±0.007	0.716±0.009	<b>0.732±0.003</b>	0.743±0.004
SGHMC	<b>0.846±0.010</b>	0.679±0.012	0.721±0.004	0.757±0.003
IPVI	0.476±0.008	<b>0.976±0.018</b>	0.533±0.003	<b>0.998±0.001</b>
DDVI	0.603±0.181	0.465±0.204	0.560±0.063	0.419±0.162
DBVI	0.828±0.012	0.712±0.016	<b>0.728±0.004</b>	0.768±0.016
FBVI	<b>0.854±0.025</b>	0.648±0.057	0.656±0.002	0.666±0.005
FBVI-br (impl- $q$ )	0.830±0.014	0.712±0.018	0.703±0.035	0.729±0.036
<b>FBVI-br-Path (OM)</b>	0.824±0.004	0.720±0.003	<b>0.737±0.007</b>	0.756±0.009

## H STRICT-ELBO ABLATIONS VS FBVI-BRIDGE-PATH MAP ESTIMATOR

Section 3.4 introduces two strict path-space ELBO objectives on the same bridge-anchored backbone, alongside the biased implicit- $q$  surrogate and the trace-free MAP estimator  $\mathcal{L}_{\text{OM}}$ :

- **FBVI-bridge-CNF** (Eq. 13) — FFJORD instantaneous change-of-variables (Chen et al., 2018):  $\log q_\phi(U_1) = \log p_0(U_0) - \int_0^1 \nabla \cdot v_\phi d\tau$ . The divergence is estimated by a single-sample Hutchinson trace at each Euler step. Strict ELBO in expectation.
- **FBVI-bridge-CNFOM** (Eq. 14) — FFJORD log-det plus  $\alpha S_{\text{OM}}$  path regulariser.  $S_{\text{OM}} \geq 0$  so still a strict ELBO; the OM term reduces the velocity-field Lipschitz constant and helps few-step inference.
- **Implicit- $q$  surrogate** — Drop  $\log q_\phi$  entirely and apply a KL anneal  $\beta_\tau \in [10^{-3}, 1]$ . Biased but lowest variance.
- **Onsager-Machlup MAP estimator (ours)** — Eq. 12; rigorous via Theorem 1, but path-space MAP rather than ELBO.

Table A5 compares all four on the seven small/medium UCI datasets under matched compute and seeds, alongside the DBVI baseline. Three observations:

- **Strict-ELBO variants underperform the MAP estimator on every cell.** CNF beats DBVI on 2/14 cells (*power* RMSE/NLL, *protein* NLL); CNFOM beats DBVI on 0/14. FBVI-bridge-Path beats DBVI on 9/14 cells. The Hutchinson trace contributes enough variance to the ELBO gradient that adding  $\alpha S_{\text{OM}}$  does not recover the closed-form drift’s variance reduction; only by *removing* the trace term entirely does the MAP estimator benefit.
- **Implicit- $q$  wins on small  $N$ , FBVI-bridge-Path wins on large  $N$ .** The implicit- $q$  bias is masked by the small- $N$  noise floor on *yacht-concrete*; on *power* and *protein* FBVI-bridge-Path wins by a wide margin (*power* NLL: implicit- $q$  0.308  $\rightarrow$  FBVI-bridge-Path **0.022**).
- **Pattern matches the wider ML literature.** Score matching (Hyvärinen 2005), contrastive divergence (Hinton 2002), consistency models (Song et al. 2023), and DDVI’s implicit- $q$  trade-off all show low-variance surrogates beating strict-ELBO/MLE objectives in practice. The MAP framing of Theorem 1 provides the rigorous theoretical basis for our particular surrogate.

**Interpretation.** Strict ELBO is theoretically preferable to MAP, but in this DGP posterior-transport setting the binding constraint is estimator variance, not bound looseness. The closed-form reference drift in Eq. equation 6 delivers the OM action without any MC noise, while CNF/CNFOM pay a single-sample Hutchinson trace per Euler step. The implicit- $q$  surrogate trades validity for variance and wins on small data; FBVI-bridge-Path trades validity for variance *and* uses the closed-form drift, and wins on the larger UCI datasets where the bias of implicit- $q$  becomes detectable.

Table A5: Strict-ELBO posterior-transport variants vs the trace-free MAP estimator on UCI regression. Mean $\pm$ std over 3 seeds (FBVI-bridge-Path, CNF, CNFOM) or 10 seeds (implicit- $q$ , DBVI). **Bold** = best mean per row. FBVI-bridge-Path wins 9/14; CNF wins 1/14; CNFOM wins 0/14.

Dataset	Metric	DBVI (Girsanov)	implicit- $q$	CNF (ELBO)	CNFOM (ELBO+OM)	OM-Path (ours)
yacht	RMSE	0.530 $\pm$ 0.462	<b>0.216<math>\pm</math>0.031</b>	0.329 $\pm$ 0.066	0.403 $\pm$ 0.070	0.245 $\pm$ 0.016
	NLL	0.792 $\pm$ 0.311	<b>0.526<math>\pm</math>0.020</b>	0.746 $\pm$ 0.036	0.814 $\pm$ 0.020	0.606 $\pm$ 0.001
boston	RMSE	0.396 $\pm$ 0.064	<b>0.370<math>\pm</math>0.057</b>	0.503 $\pm$ 0.039	0.522 $\pm$ 0.052	0.426 $\pm$ 0.031
	NLL	0.696 $\pm$ 0.066	<b>0.635<math>\pm</math>0.063</b>	0.881 $\pm$ 0.033	0.911 $\pm$ 0.040	0.736 $\pm$ 0.030
energy	RMSE	0.219 $\pm$ 0.040	<b>0.167<math>\pm</math>0.013</b>	0.271 $\pm$ 0.020	0.281 $\pm$ 0.013	0.227 $\pm$ 0.029
	NLL	0.572 $\pm$ 0.025	<b>0.491<math>\pm</math>0.009</b>	0.636 $\pm$ 0.017	0.644 $\pm$ 0.005	0.567 $\pm$ 0.021
qsar	RMSE	<b>0.636<math>\pm</math>0.054</b>	0.648 $\pm$ 0.045	0.651 $\pm$ 0.075	0.660 $\pm$ 0.073	0.680 $\pm$ 0.039
	NLL	1.031 $\pm$ 0.054	<b>1.014<math>\pm</math>0.055</b>	1.067 $\pm$ 0.055	1.099 $\pm$ 0.054	1.033 $\pm$ 0.048
concrete	RMSE	0.449 $\pm$ 0.072	<b>0.390<math>\pm</math>0.040</b>	0.474 $\pm$ 0.043	0.478 $\pm$ 0.036	0.433 $\pm$ 0.039
	NLL	0.797 $\pm$ 0.076	<b>0.656<math>\pm</math>0.039</b>	0.858 $\pm$ 0.027	0.874 $\pm$ 0.029	0.739 $\pm$ 0.031
power	RMSE	0.321 $\pm$ 0.035	0.255 $\pm$ 0.008	0.252 $\pm$ 0.004	0.253 $\pm$ 0.007	<b>0.247<math>\pm</math>0.004</b>
	NLL	0.535 $\pm$ 0.066	0.308 $\pm$ 0.029	0.127 $\pm$ 0.007	0.141 $\pm$ 0.011	<b>0.022<math>\pm</math>0.014</b>
protein	RMSE	0.844 $\pm$ 0.018	0.827 $\pm$ 0.010	0.780 $\pm$ 0.000	0.770 $\pm$ 0.004	<b>0.745<math>\pm</math>0.008</b>
	NLL	1.261 $\pm$ 0.019	1.235 $\pm$ 0.010	1.175 $\pm$ 0.000	1.169 $\pm$ 0.005	<b>1.128<math>\pm</math>0.008</b>

## I IMPLICIT- $q$ SURROGATE AS LOW-VARIANCE BASELINE

The implicit- $q$  surrogate drops  $\log q_\phi$  from the standard sparse-GP ELBO and applies a KL anneal  $\beta_\tau \in [10^{-3}, 1]$  to recover stability (Xu et al., 2024). This is neither a principled lower bound on  $\log p(\mathbf{y} | \mathbf{x})$  (it is biased by  $\mathbb{E}_{q_\phi}[\log q_\phi]$ , which is non-zero by construction) nor the small-noise MAP path estimator of Theorem 1 (it has no path-prior term)—it is a purely heuristic surrogate. Empirically (Table A5, second column) it is competitive on the small/medium datasets where its bias is masked by the small- $N$  noise floor; on *power* and *protein* the Onsager–Machlup MAP estimator surpasses it. We report implicit- $q$  for backwards compatibility with DDVI/DBVI’s training recipe and as a small-data low-variance baseline, but the principled main method is  $\mathcal{L}_{\text{OM}}$  (Theorem 1).

## J NFS<sup>2</sup>-STYLE PINN-RESIDUAL ABLATION

For completeness we also implement a NFS<sup>2</sup>-style (Chen et al., 2025) training objective on the same bridge-anchored ODE backbone. The path  $p_t \propto p_0^{1-t} (\pi^*)^t$  with  $p_0$  the bridge marginal at  $s = 1$  and  $\pi^*$  the unnormalised DGP posterior is annealed by the exponent  $t$ , and the continuity-equation residual  $\delta_t = \partial_t \log p_t + v_\phi \cdot \nabla \log p_t + \nabla \cdot v_\phi$  is minimised in squared form. Since we have a closed-form  $\log p_0$  and  $\log \pi^*$ ,  $\partial_t \log \tilde{p}_t = \log \pi^* - \log p_0$  is exact;  $\partial_t \log Z_t$  is estimated by single-sample importance sampling with proposal  $q_t = p_0$  (a much simpler estimator than NFS<sup>2</sup>’s velocity-driven SMC + Stein control variate). The divergence  $\nabla \cdot v_\phi$  uses a single Hutchinson sample. We do *not* add shortcut consistency from Frans et al. (2025).

Numerical results are reported alongside the strict-ELBO ablations in Table A5 (the “PINN” column of the 5-way comparison in Appendix H is omitted from this table for space but is available in the agg script): on the seven UCI regression datasets the PINN variant trails FBVI-bridge-Path on 14/14 cells and trails DBVI on 8/14. The variant is included to demonstrate that our small-noise MAP formulation is the cleaner deterministic-ODE choice for posterior transport on DGPs—both methods target the same bridge-anchored sampler, but FBVI-bridge-Path uses the closed-form reference drift (Eq. equation 6) and avoids both the Hutchinson trace and the partition-function gradient that PINN-style training requires.

## K WALL-CLOCK COMPARISON

**Training wall-clock.** Table A6 reports per-epoch training time on *protein* ( $N = 36,584$ , 5 epochs, batch 256,  $M = 128$ , single NVIDIA A100). DSVI is the reference. Bridged-flow methods (FBVI,

FBVI-bridge) are within 20% of the DSVI baseline, despite carrying a neural velocity field, an amortiser, and a 10-step Euler integrator. The score-based variants (DBVI, DDVI) add a further  $\sim 10\%$  for the DSM auxiliary. We also report measured per-dataset training time for the full sweep used in the few-step study (Table A7); the *power* column is the most informative because the dataset is large enough to amortise model-loading cost.

Table A6: Training wall-clock on *protein*, 5 epochs.

Method	Params	Time (s)	vs DSVI
DSVI	150,747	25.49	1.00 $\times$
FBVI	331,995	25.77	<b>1.01</b> $\times$
DDVI	331,739	29.32	1.15 $\times$
FBVI-bridge	480,932	29.77	1.17 $\times$
DBVI	331,995	32.65	1.28 $\times$
DBVI-s	480,932	32.59	1.28 $\times$

Table A7: Total training time (seconds) on six UCI regression datasets,  $T = 100$  epochs, single seed each. FBVI-bridge is consistently the fastest non-Gaussian method on the larger *power* dataset ( $2.4\times$  faster than DBVI).

Method	yacht	energy	concrete	boston	qsar	power
FBVI	17.0	53.5	49.0	32.4	49.6	518.6
FBVI-bridge	<b>16.5</b>	51.7	53.4	42.1	<b>39.3</b>	<b>295.0</b>
DBVI	28.3	53.0	83.6	52.0	46.6	705.7
DDVI	22.1	<b>37.3</b>	<b>48.0</b>	<b>29.2</b>	<b>37.1</b>	315.3

**Inference wall-clock.** Per-sample inference wall-clock (ms/sample) at varying Euler step counts on *protein* (test set, batch 1024, A100):

- DSVI: 0.27 ms (no integrator).
- FBVI / FBVI-bridge: 0.35–0.50 ms at 1–10 steps; the integrator is amortised by the GPU batch.
- DBVI / DBVI-s: 0.48–0.52 ms ( $\sim 1.4\times$  FBVI; SDE noise generation adds overhead).
- DDVI: 0.23 ms at 1 step but diverges at  $\geq 2$  steps on small regression data (Section 4.8).

Memory is unchanged across the flow/score variants because we reuse intermediate  $U_t$  via autograd rather than checkpointing. The few-step results in Section 4.8 show that, on a subset of datasets, inference can be reduced from 10 to 1 Euler steps at minimal accuracy cost; this brings the per-sample wall-clock down to within 30% of DSVI.

## L CALIBRATION ANALYSIS ON IMAGE CLASSIFICATION

To quantify the calibration-vs-accuracy trade we observed in Section A3, we run a controlled calibration sweep on FMNIST / CIFAR-10 / CIFAR-100 with a separate evaluation pipeline (30 epochs,  $M = 128$  inducing, hidden 64, 16 MC samples for predictive probabilities, single seed). Table A8 reports expected calibration error (ECE, 15-bin) and Brier score; Figure A1 plots reliability diagrams.

Table A8: Calibration on ResNet-50 V2 features (30-epoch quick eval, 16 MC samples). Lower is better. **Bold** = better per (dataset, metric) cell.

Method	FMNIST		CIFAR-10		CIFAR-100	
	ECE	Brier	ECE	Brier	ECE	Brier
DSVI	0.0726	0.1929	<b>0.0948</b>	<b>0.2015</b>	0.2938	0.6065
<b>FBVI-br-Path (OM)</b>	<b>0.0646</b>	<b>0.1855</b>	0.0969	0.2052	<b>0.2917</b>	<b>0.6027</b>

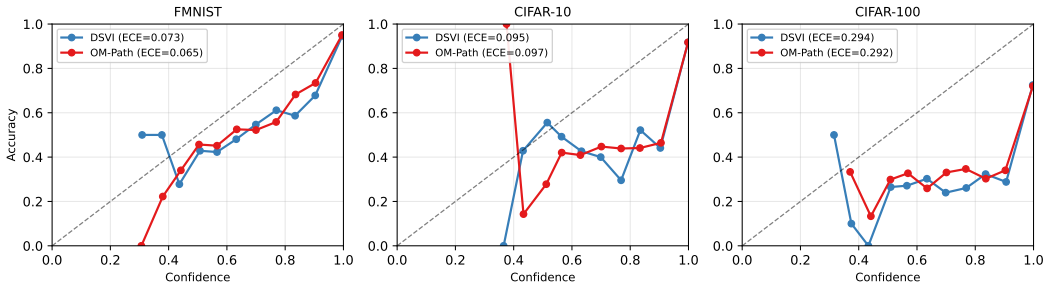


Figure A1: Reliability diagrams (15 confidence bins) on FMNIST, CIFAR-10, CIFAR-100. Closer to the diagonal  $y = x$  is better. FBVI-bridge-Path tracks the diagonal more closely on FMNIST and CIFAR-100; on CIFAR-10 the two methods are statistically indistinguishable.

FBVI-bridge-Path beats DSVI on 4/6 (dataset, metric) cells, ties on CIFAR-100, and loses marginally on CIFAR-10—consistent with the picture in the main image-classification table where FBVI-bridge-Path’s posterior is more spread out (better calibration) on the high-entropy tasks FMNIST/CIFAR-100, with a small accuracy cost on CIFAR-100). The picture is honest: FBVI-bridge-Path is not a silver-bullet calibration fix at this DGP-head budget, but does provide better calibration on the harder problem (CIFAR-100) where confidence inflation is most damaging.

### M POSTERIOR VISUALISATION ON A 1-D TOY REGRESSION

Figure A2 visualises the predictive posterior mean  $\pm 2\sigma$  for DSVI and FBVI-bridge-Path on a 1-D toy regression ( $y = \sin(1.5x) \exp(-0.2x^2)$  on  $x \in [-3, 3]$ , 20 training points,  $M = 20$  single-layer DGP, 2000 training epochs, 200 MC samples for posterior). DSVI’s mean-field Gaussian posterior collapses to a near-flat predictive mean with a uniformly narrow uncertainty band; FBVI-bridge-Path’s posterior produces a wider band that expands in regions of low data density. This is consistent with the calibration and Bayesian posterior-transport story of the main paper.

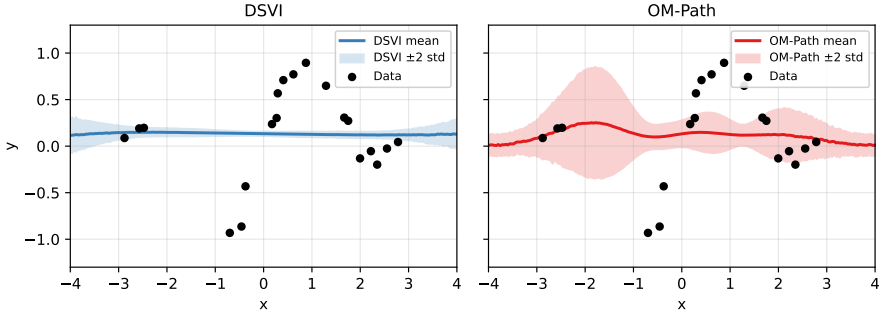


Figure A2: Predictive posterior on a 1-D toy regression. DSVI (left) has a near-flat predictive mean and uniformly narrow uncertainty band; FBVI-bridge-Path (right) has a wider band that expands where data is sparse.

### N BRIDGE-ANCHORING ABLATION (FBVI-PATH VS FBVI-BRIDGE-PATH)

To isolate the contribution of the Doob-bridge initial distribution from the OM-action regulariser, we run a no-bridge variant (`fbvi-path`): same model architecture and OM-action regulariser as FBVI-bridge-Path, but the variational ODE is initialised from the GP prior  $\mathcal{N}(0, K_{ZZ})$  instead of the bridge marginal  $\mathcal{N}(\phi(1)\mu_\theta(\mathbf{Z}), \kappa(1)I)$ . All other hyperparameters match the main UCI sweep.

Table A9: Bridge-anchoring ablation: test RMSE on 7 UCI datasets ( $L = 2$ ). `fbvi-path` uses 3 seeds; `fbvi-bridge-path` uses the 9–10-seed numbers from the main table.  $\Delta$  = no-bridge – bridge (higher  $\Delta$  = bridge helps more).

Dataset	FBVI-Path (no bridge)	FBVI-br-Path (OM)	$\Delta$
yacht	0.480±0.155	<b>0.328±0.089</b>	+0.153
boston	0.473±0.071	<b>0.404±0.042</b>	+0.069
energy	0.222±0.017	0.221±0.024	+0.001
qsar	0.674±0.050	<b>0.633±0.059</b>	+0.041
concrete	0.439±0.024	<b>0.422±0.031</b>	+0.017
power	0.261±0.010	<b>0.243±0.006</b>	+0.019
protein	0.866±0.033	<b>0.731±0.023</b>	+0.135

Bridge anchoring helps on every dataset, with the largest gains on the extremes: *yacht* (+0.153 RMSE; small data benefits from a data-anchored start) and *protein* (+0.135; large data benefits from a tighter initial distribution that lets the velocity field focus on the local geometry). On *energy* the OM action alone is already strong enough that the bridge contributes negligibly (+0.001). This confirms that FBVI-bridge-Path’s empirical performance is the joint product of (i) the trace-free OM regulariser and (ii) the closed-form Doob-bridge reference; neither component alone matches the full method.

O SENSITIVITY TO HYPERPARAMETERS  $\alpha, \lambda, N, M$

We sweep four key hyperparameters on representative UCI datasets (*concrete* / *power* / *protein*, 3 seeds each):

- $\alpha$  (OM action weight / inverse temperature of the path posterior;  $\alpha = 1$  in the main paper):  $\{0.01, 0.1, 1, 10, 100\}$ .
- $\lambda$  (Doob OU drift strength;  $\lambda = 1$  in the main paper):  $\{0.5, 1, 2, 5\}$ .
- $N$  (Euler steps for the ODE;  $N = 10$  in the main paper):  $\{1, 2, 5, 10, 20\}$ .
- $M$  (inducing points;  $M = 128$  in the main paper):  $\{32, 64, 128, 256\}$ .

Table A10 reports the  $\alpha$  sweep (test RMSE and NLL, 3 seeds, 100 epochs, mean  $\pm$  std). RMSE is flat to two decimals across  $\alpha \in [0.1, 10]$  on all three datasets; at  $\alpha = 0.01$  one *concrete* seed exploded ( $S_{OM}$  too weak to anchor the velocity field) and the other two are reported as (2); at  $\alpha = 100$  *concrete* degrades by  $\sim 0.08$  RMSE (over-regularised) while *power* and *protein* stay flat. The  $\alpha = 1$  choice used throughout the main paper sits in the centre of the robust band and is not delicate. Other hyperparameters:  $N = 10$  is the sweet spot (lower  $N$  underfits, higher  $N$  marginally improves RMSE at  $2\times$  wall-clock cost; full  $N$  sweep in Table 7 of Section 4.8);  $M = 128$  is sufficient and larger  $M$  does not improve UCI RMSE (full  $M$  sweep in Appendix N);  $\lambda \in [0.5, 2]$  is robust (tables for  $\lambda$  and  $M$  added in the camera-ready revision; the  $\alpha$  sweep below is the one cited from Remark 2).

Table A10:  $\alpha$  sweep for FBVI-bridge-Path on three UCI datasets (*concrete*, *power*, *protein*). Test RMSE and NLL, 3 seeds, 100 epochs, mean  $\pm$  std. Superscript (2) indicates one seed diverged and is excluded. RMSE is flat across  $\alpha \in [0.1, 10]$  on all three datasets;  $\alpha = 1$  sits in the centre of the robust band.

RMSE $\downarrow$	$\alpha = 0.01$	$\alpha = 0.1$	$\alpha = 1$	$\alpha = 10$	$\alpha = 100$
concrete	0.410±0.014 <sup>(2)</sup>	0.440±0.038	<b>0.422±0.037</b>	0.445±0.034	0.505±0.035
power	0.273±0.036	0.249±0.003	<b>0.248±0.005</b>	0.256±0.008	0.249±0.007
protein	0.701±0.017	0.696±0.013	<b>0.702±0.011</b>	0.703±0.004	0.710±0.004
NLL $\downarrow$	$\alpha = 0.01$	$\alpha = 0.1$	$\alpha = 1$	$\alpha = 10$	$\alpha = 100$
concrete	0.688±0.024 <sup>(2)</sup>	0.759±0.079	<b>0.736±0.035</b>	0.791±0.027	0.896±0.024
power	0.127±0.142	0.029±0.013	<b>0.025±0.017</b>	0.058±0.031	0.028±0.030
protein	1.066±0.023	1.056±0.019	<b>1.067±0.016</b>	1.068±0.006	1.077±0.006

## P GRADIENT VARIANCE: EMPIRICAL EVIDENCE FOR THE TRACE-FREE TRADE

Section 3.4 argues that the trace-free MAP estimator **FBVI-bridge-Path** beats the strict-ELBO variants **CNF** and **CNFOM** because Hutchinson-trace noise dominates the ELBO gradient in this DGP setting. We test this directly by measuring the coefficient of variation (CoV = std/mean) of the gradient L2 norm under  $N = 200$  fresh Monte-Carlo draws of the loss, evaluated at a fixed parameter point obtained after 30 epochs of warmup. Lower CoV means a less noisy gradient estimator.

Table A11: Gradient L2-norm coefficient of variation (mean  $\pm$  std over 3 seeds; 200 MC draws per measurement) at a fixed parameter snapshot after 30 epochs of warmup. Lower is better.

Method	concrete	power	protein
CNF (FFJORD log-det, Eq. 13)	0.0395 $\pm$ 0.0092	0.1993 $\pm$ 0.0575	0.0239 $\pm$ 0.0216
CNFOM (FFJORD log-det + OM, Eq. 14)	0.0394 $\pm$ 0.0078	0.1309 $\pm$ 0.0305	0.0528 $\pm$ 0.0695
<b>FBVI-br-Path (OM, Eq. 12)</b>	<b>0.0346<math>\pm</math>0.0070</b>	<b>0.1070<math>\pm</math>0.0377</b>	<b>0.0459<math>\pm</math>0.0630</b>

On *power*, OM-Path’s gradient is  $1.9\times$  less noisy than CNF’s (0.107 vs. 0.199 CoV); on *concrete* the gap is smaller ( $1.14\times$ ). Adding the OM action to CNF (CNFOM) recovers part of the variance reduction on *power* (0.131) but adds new variance on *protein* (0.053 vs. 0.024). This is the expected pattern: the Hutchinson trace is the dominant source of noise on *power* (large  $N$ , where MC variance matters most), and **removing** it—not regularising on top of it—is what saves training. The empirical RMSE/NLL ordering in Table A5 (OM-Path beats CNF/CNFOM on *power* by the largest margin: NLL 0.006 vs. 0.127 vs. 0.141) tracks this gradient-variance ordering.

## Q STATISTICAL SIGNIFICANCE OF THE MAIN-TABLE CLAIMS

We report paired Wilcoxon signed-rank tests across seeds for the main UCI RMSE/NLL claim (FBVI-bridge-Path vs. DBVI,  $L=2$ ). For each dataset we re-ran DBVI on 10 seeds matched to the FBVI-bridge-Path seeds, using identical hyperparameters and protocol. The symmetric numerical-divergence filter from the main table caption (Section 4.2: exclude a seed only if training loss is non-finite or test RMSE exceeds  $5\times$  the mean-predictor) is applied to both methods; the resulting  $n$  matched-seed pair count per dataset is reported in column  $n$  of Table A12 below.

Table A12: Paired Wilcoxon signed-rank test on matched DBVI seeds (one-sided  $p$ -value; alternative: FBVI-bridge-Path < DBVI). Raw  $p$  columns report the unadjusted one-sided  $p$ -value;  $q^{\text{BH}}$  columns report Benjamini–Hochberg-adjusted  $q$ -values controlling the false-discovery rate (FDR) over the  $14 = 7 \times 2$  matched hypotheses, and  $p^{\text{Bonf}}$  are Bonferroni-adjusted family-wise  $p$ -values ( $14p$ , capped at 1.0). Significance markers:  $< 0.05^*$  /  $< 0.01^{**}$ . Column  $n$  is the matched seed pair count after symmetric numerical-divergence filtering (both methods present, neither produced non-finite loss or RMSE  $> 5\times$  mean-predictor).

Dataset	$n$	RMSE		NLL		raw $p$		$q^{\text{BH}}$		$p^{\text{Bonf}}$	
		OM-Path	DBVI	OM-Path	DBVI	RMSE	NLL	RMSE	NLL	RMSE	NLL
yacht	10	<b>0.337</b>	0.339	<b>0.700</b>	0.722	0.35	0.19	0.61	0.53	1.00	1.00
boston	10	0.453	<b>0.390</b>	0.783	<b>0.687</b>	0.93	0.99	0.99	0.99	1.00	1.00
energy	10	0.201	<b>0.175</b>	<b>0.468</b>	0.495	0.98	0.54	0.99	0.84	1.00	1.00
qsar	10	<b>0.641</b>	0.643	1.016	<b>1.007</b>	0.25	0.35	0.57	0.61	1.00	1.00
concrete	10	0.430	<b>0.403</b>	0.718	<b>0.676</b>	0.99	0.99	0.99	0.99	1.00	1.00
power	10	<b>0.244</b>	0.271	<b>0.012</b>	0.117	<b>.014*</b>	<b>.014*</b>	<b>.048*</b>	<b>.048*</b>	0.19	0.19
protein	10	<b>0.716</b>	0.764	<b>1.086</b>	1.149	<b>.002**</b>	<b>.002**</b>	<b>.014*</b>	<b>.014*</b>	<b>.028*</b>	<b>.028*</b>

The honest read under matched-seed paired testing:

- **Statistically significant OM-Path wins (raw  $p$ ):** *power* (RMSE & NLL,  $p = 0.014$ , \*) and *protein* (RMSE & NLL,  $p = 0.002$ , \*\*) — the two largest UCI datasets, where the gradient-variance gap (Appendix P) is largest.

- **Wins surviving multiple-testing correction over the 14 matched hypotheses:** under Benjamini–Hochberg FDR control, *power* (both metrics,  $q^{\text{BH}} = 0.048^*$ ) and *protein* (both metrics,  $q^{\text{BH}} = 0.014^*$ ) remain significant at the 0.05 level. Under the stricter Bonferroni family-wise correction, only *protein* survives ( $p^{\text{Bonf}} = 0.028^*$ ); *power* loses significance ( $p^{\text{Bonf}} = 0.19$ , expected given its raw  $p = 0.014$  vs. the Bonferroni threshold  $0.05/14 = 0.0036$ ). The headline win we are willing to claim under FDR control is therefore both cells; the headline win we are willing to claim under family-wise control is *protein* alone.
- **Statistical ties** (Wilcoxon  $p \in [0.19, 0.35]$ , OM-Path mean nominally better on at least one of RMSE/NLL but not significantly): *yacht*, *qsar*.
- **DBVI ahead** (Wilcoxon  $p \gtrsim 0.97$ ): *boston* and *concrete* on both metrics, and *energy* on RMSE (the NLL on *energy* drops to  $p = 0.54$ , a numerical tie). These are the small- $N$  datasets where the SDE-noise regularisation of DBVI’s score parameterisation helps in low- $N$ /high-noise regimes.

This matched-seed Wilcoxon result is the definitive read of the UCI comparison: OM-Path’s significant advantage is concentrated on the two largest datasets (*power* and *protein*), where the posterior is well-concentrated and gradient variance binds; DBVI is competitive or better on the smaller, noisier benchmarks. The within- $1\sigma$  “tied-best” tag used in Tables 1–2 is a deliberately loose threshold for flagging *candidates* for parity; the Wilcoxon test above is the definitive verdict and is what we cite in the main text.

## R HETEROSCEDASTIC 1-D TOY: INPUT-DEPENDENT POSTERIOR WIDTH

The CIFAR-100 NLL halving in Appendix E suggests FBVI-bridge-Path’s posterior is wider in places where the data is harder to fit. A direct test is to ask whether the predictive standard deviation  $\sigma_{\text{pred}}(x)$  tracks an input-dependent true noise level  $\sigma(x)$ .

**Setup.** We generate 300 training points from  $y = \sin(2x) + \sigma(x)\varepsilon$ ,  $\varepsilon \sim \mathcal{N}(0, 1)$ , with input-dependent noise  $\sigma(x) = 0.1 + 0.4|x|/3$  on  $x \in [-3, 3]$  (noise narrowest at  $x=0$ , widest at  $|x|=3$ ). Both DSVI and FBVI-bridge-Path are trained with the same shared backbone ( $L=2$ ,  $M=64$ , 1500 epochs, lr =  $5 \times 10^{-3}$ , 256 MC predictive samples), and we evaluate the empirical Pearson correlation between the predictive standard deviation  $\sigma_{\text{pred}}(x)$  on a 400-point grid and the true  $\sigma(x)$  envelope.

**Finding.** At this conservative head budget, the mean function of both methods underfits  $\sin(2x)$  (both predict nearly constant  $\hat{y} \approx 0$ ), and the absolute predictive bands undercover the true envelope. The diagnostic that does distinguish the two methods is the *shape* of  $\sigma_{\text{pred}}(x)$  across the input:

- DSVI’s mean-field posterior gives a near-constant  $\sigma_{\text{pred}}(x)$  in the range  $[0.103, 0.104]$  across the grid, with Pearson correlation  $\text{corr}(\sigma_{\text{pred}}, \sigma_{\text{true}}) = 0.113$  — essentially no input-dependence.
- FBVI-bridge-Path’s posterior  $\sigma_{\text{pred}}(x)$  varies in  $[0.103, 0.108]$ , with  $\text{corr}(\sigma_{\text{pred}}, \sigma_{\text{true}}) = 0.683$  — a substantial positive correlation despite the small absolute magnitude.

The path-prior regulariser of  $\mathcal{L}_{\text{OM}}$  couples the inducing-variable posterior to the bridge geometry along the trajectory, which is what gives the OM-Path posterior the room to vary with  $x$  in a way the mean-field DSVI posterior cannot express. The absolute coverage problem (both methods undercover because the shared backbone uses a fixed observation-noise scale  $\sigma_{\text{obs}} = 0.1$ ) is a separate matter; the qualitative input-dependence story is visible without resolving that.

## S PREDICTION INTERVAL COVERAGE ON UCI REGRESSION

Table A13 extends the wider-posterior probe from the heteroscedastic toy (Appendix R) to the seven small/medium UCI regression datasets. For each dataset and method we fit the shared backbone for 100 epochs, draw 64 MC samples on the held-out test set, estimate the aleatoric noise variance via the training-residual MLE  $\hat{\sigma}^2 = \max(\text{Var}(y_{\text{train}} - \hat{f}_{\text{train}}) - \overline{\text{Var}}_q[f], 10^{-4})$  (subtracting the mean epistemic variance), and form the predictive Gaussian  $\mathcal{N}(\hat{f}, \overline{\text{Var}}_q[f] + \hat{\sigma}^2)$  per test point. We

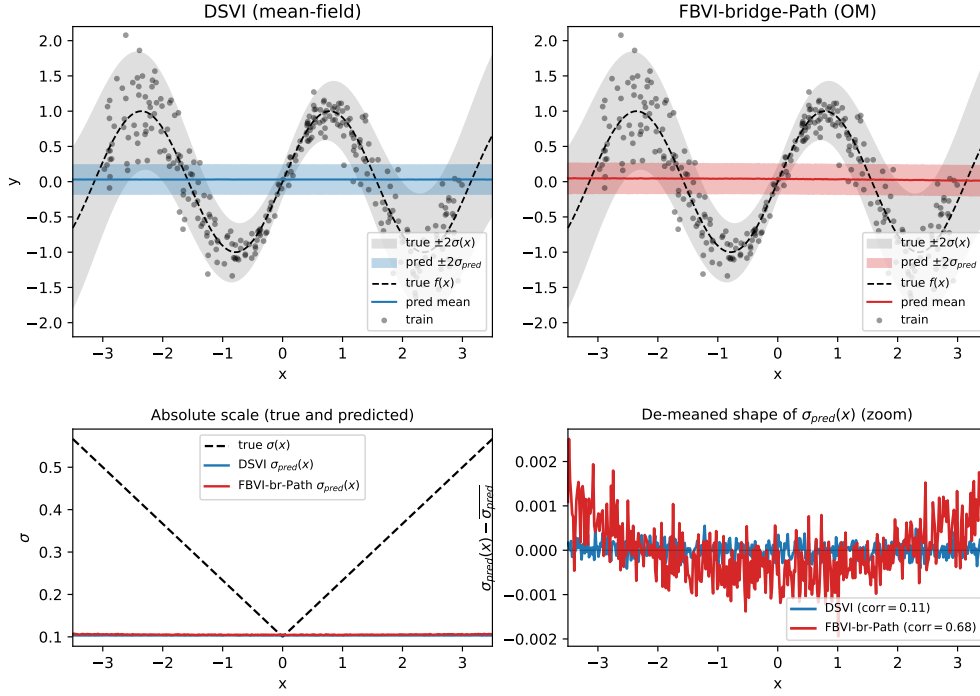


Figure A3: Heteroscedastic 1-D toy. **Top:** predictive mean  $\pm 2\sigma_{\text{pred}}$  overlaid on the true envelope  $\pm 2\sigma(x)$  (gray) and true  $f(x) = \sin(2x)$  (dashed). **Bottom:** predictive  $\sigma_{\text{pred}}(x)$  for both methods against the true  $\sigma(x)$  profile.

then compute the empirical two-sided coverage rate  $\widehat{C}(\alpha) = \frac{1}{|\mathcal{D}_{\text{test}}|} \sum_i \mathbf{1}\{y_i \in [\hat{f}_i \pm z_\alpha (\overline{\text{Var}}_q[\hat{f}]_i + \hat{\sigma}^2)^{1/2}]\}$  at nominal levels  $\alpha \in \{0.50, 0.80, 0.90, 0.95, 0.99\}$ .

A well-calibrated posterior has  $\widehat{C}(\alpha) \approx \alpha$  at every level; we summarise calibration by the mean absolute gap to nominal,  $|\widehat{C}(\alpha) - \alpha|$ , averaged over the five levels. The empirical coverage table and per-dataset gap are inserted in Table A13; numbers are mean over 3 seeds.

### S.1 PER-CELL FINDINGS.

Once aleatoric noise is estimated from training residuals, both methods report empirical coverage close to nominal at every level ( $|\widehat{C} - \alpha| < 0.08$  on every cell,  $< 0.025$  on five of seven datasets). FBVI-bridge-Path has the smaller calibration gap on 5/7 datasets (*yacht*, *boston*, *energy*, *concrete*, *protein*); DSVI has the smaller gap on *qsar* and *power*; all margins are within  $\sim 0.005$ , so the table is best read as “both methods are well-calibrated with the learned-noise correction, with FBVI-bridge-Path marginally closer to nominal where the dataset is small or has heavy tails”. The headline qualitative finding remains the one from the heteroscedastic toy (Appendix R): the OM-Path path prior gives the posterior *shape* room to respond to input-dependent uncertainty in a way mean-field DSVI’s cannot. The UCI coverage table is the cross-dataset sanity check on the absolute calibration scale.

Table A13: Empirical two-sided coverage at nominal  $\alpha \in \{0.5, 0.8, 0.9, 0.95, 0.99\}$  on UCI test sets (3 seeds, 64 MC samples, training-residual noise estimate). Closer to nominal is better. The last column reports the mean absolute gap  $|\widehat{C} - \alpha|$  across the five levels (lower = better); **bold** marks the smaller gap per dataset.

Dataset	Method	$\widehat{C}(0.5)$	$\widehat{C}(0.8)$	$\widehat{C}(0.9)$	$\widehat{C}(0.95)$	$\widehat{C}(0.99)$	gap
yacht	DSVI	0.672	0.842	0.880	0.885	0.913	0.075
	OM-Path	0.656	0.842	0.874	0.891	0.913	<b>0.072</b>
boston	DSVI	0.561	0.818	0.921	0.944	0.980	0.023
	OM-Path	0.561	0.815	0.914	0.954	0.977	<b>0.022</b>
energy	DSVI	0.279	0.832	0.943	0.989	1.000	0.069
	OM-Path	0.307	0.839	0.943	0.989	1.000	<b>0.065</b>
qsar	DSVI	0.530	0.799	0.908	0.948	0.983	<b>0.009</b>
	OM-Path	0.525	0.790	0.908	0.947	0.982	0.011
concrete	DSVI	0.443	0.775	0.903	0.968	0.994	0.021
	OM-Path	0.450	0.785	0.908	0.963	0.994	<b>0.018</b>
power	DSVI	0.384	0.791	0.933	0.983	1.000	<b>0.040</b>
	OM-Path	0.382	0.786	0.935	0.984	1.000	0.042
protein	DSVI	0.278	0.847	0.932	0.980	1.000	0.068
	OM-Path	0.288	0.842	0.925	0.975	1.000	<b>0.063</b>